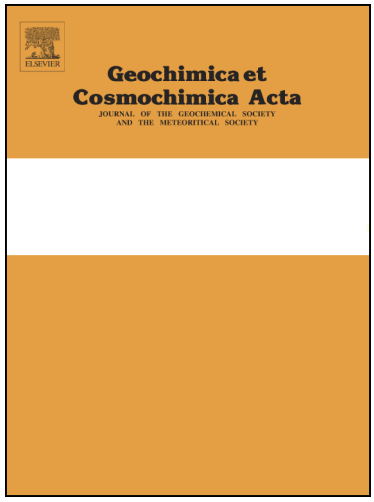

Geochemistry of dissolved aluminum at low pH: Extent and significance of Al-Fe$^{(III)}$ coprecipitation below pH 4.0

Javier Sánchez-España, Iñaki Yusta, Jennifer Gray, William D. Burgos

PII: S0016-7037(15)00660-2
DOI: http://dx.doi.org/10.1016/j.gca.2015.10.035
Reference: GCA 9511

To appear in: *Geochimica et Cosmochimica Acta*

Received Date: 21 March 2015
Accepted Date: 28 October 2015

Please cite this article as: Sánchez-España, J., Yusta, I., Gray, J., Burgos, W.D., Geochemistry of dissolved aluminum at low pH: Extent and significance of Al-Fe$^{(III)}$ coprecipitation below pH 4.0, *Geochimica et Cosmochimica Acta* (2015), doi: http://dx.doi.org/10.1016/j.gca.2015.10.035

Geochemistry of dissolved aluminum at low pH: Extent and significance of Al-Fe$^{(III)}$ coprecipitation below pH 4.0

Javier Sánchez-España[(1)], Iñaki Yusta[(2)], Jennifer Gray[(3)], William D. Burgos[(4)]

(1) Unidad de Mineralogía e Hidrogeoquímica Ambiental (UMHA), Instituto Geológico y Minero de España (IGME), Calera, 1, 28760 Tres Cantos, Madrid, Spain (j.sanchez@igme.es)
(2) Unidad de Mineralogía e Hidrogeoquímica Ambiental (UMHA), Departamento de Mineralogía y Petrología, Facultad de Ciencia y Tecnología, Universidad del País Vasco (UPV/EHU), Apdo. 644, E-48080 Bilbao, Spain
(3) Materials Research Institute, The Pennsylvania State University, N-022 Millennium Science Complex, University Park 16802-1408, State College, PA
(4) Department of Civil and Environmental Engineering, The Pennsylvania State University, 212 Sacket Building, University Park 16802-1408, State College, PA

Abstract – This work examines the geochemical behaviour of dissolved aluminum in sulfate-rich acidic waters. Our observations were obtained during several years of geochemical and mineralogical research in the San Telmo acidic pit lake and other pit lakes of SW Spain. The work includes scanning and transmission electron microscopy (SEM, TEM) of suspended mineral colloids found in deep lake waters. Energy dispersion spectroscopy (EDS) coupled to scanning and high resolution transmission electron microscopy (STEM, HRTEM) revealed not only the presence and formation of discrete, sub-micron Al solids like alunite, but also the abundance and distribution of Al into Fe(III) phases typical of acid mine drainage, such as schwertmannite and jarosite, at a nanometric resolution. The main conclusion emerging from our work is that the fate and transport of Al at low pH (<4.0) can be largely influenced by adsorption on and/or coprecipitation with both schwertmannite and jarosite. Under the geochemical conditions studied (SO_4^{2-}=10^{-2} M, Fe(III)~Al=10^{-3} M), alunite formation may occur at pH>3.3, as suggested by mineralogical observations and geochemical modelling. Below this pH, and contrary to the extended assumption, Al is not truly conservative, and in the presence of ferric iron, both metals may co-precipitate at a substantial extent to form either particles of Al-rich schwertmannite (containing up to ca. 8 at.% Al with [Fe/(Fe+Al)]=0.77) and/or crystals of H_3O^+- to K^+-jarosite (containing up to ca. 10 at.% Al with [Fe/(Fe+Al)]=0.54). This Al incorporation seems to take place by adsorption on particle surfaces in schwertmannite and by atomic substitution for Fe^{3+} in jarosite. Alunite is also unstable at this low pH range with respect to jarosite, which may lead either to isomorphic transformation and/or to chemically zoned crystals with jarositic rims around previously formed alunite cores. As a whole, the compositional spectrum of the analysed jarosites and alunites describes a discontinuous, coupled (Al^{3+}-Fe^{3+}, H_3O^+-K^+) solid solution series with an apparent gap at intermediate compositions. However, this gap seems to follow geochemical aspects more than crystallographic factors (i.e., immiscibility). The combination of this macroscopically *invisible* Al incorporated into Fe(III) solids along with subordinate alunite formation may cause significant Al removal even at very low pH (e.g., 20% decrease in Al concentration in San Telmo at pH<3.1). Furthermore, this Fe(III)-Al co-precipitation may also affect the fate of toxic trace elements like As and Pb.

1. INTRODUCTION

Aluminum is present in acidic waters around the world. The main source of aluminum in these environments is the dissolution of aluminosilicates (*e.g.*, feldspar; reaction 1):

$$KAlSi_3O_8 + 4H^+ + 4H_2O \leftrightarrow Al^{3+} + 3Si(OH)_4 + K^+ \quad (1)$$

The release of Al may be enhanced during microbially-mediated pyrite oxidation by the generation of sulfuric acid (Nordstrom and Alpers, 1999; Bigham and Nordstrom, 2000). Given its high toxicity to many organisms (*e.g.*, Garciduenas and Cervantes, 1996), the geochemical behaviour of aluminum in aquatic systems has been widely studied. In particular, the geochemistry of aluminum in acidic waters (*e.g.*, mine waters) and soils has been addressed in numerous studies (*e.g.*, Van Bremen et al., 1973; Nordstrom, 1982; Nordstrom and Ball, 1986; Karathanasis et al., 1988; Lindsay and Walthall, 1996; Nordstrom and Alpers, 1999; Bigham and Nordstrom, 2000; Sánchez-España, 2007; Jones et al., 2011). Dissolved aluminum in fresh waters is mostly present in the form of Al-OH species (*e.g.*, $Al(OH)^{2+}$, $Al(OH)_2^+$). Below pH<5.0, aluminum is usually considered to remain in solution and, above this pH, to precipitate as Al hydroxides such as gibbsite or amorphous $Al(OH)_3$. In contrast, aluminum speciation in acid mine drainage (AMD) is strongly influenced by the high concentration of sulfate (SO_4^{2-}) such that sulfate complexes (*i.e.*, $AlSO_4^+$, $Al(SO_4)^{2-}$) are predominant compared to Al^{3+}.

Aluminum buffers many acidic (pit) lakes, where experimental and modelling work has shown that Al^{3+} may precipitate at pH>4.0 near the lake bottom (Sánchez-España et al., 2011). At this pH value, nanocrystalline oxyhydroxysulfate minerals such as felsőbányaite (or its more hydrated precursor, hydrobasaluminite) may form by reaction 2:

$$4Al^{3+} + SO_4^{2-} + 14\ H_2O \leftrightarrow Al_4(SO_4)(OH)_{10}\cdot 4H_2O + 10H^+ \quad (2)$$

The formation of these colloidal solids has been widely observed in acidic surface waters of the Iberian Pyrite Belt (IPB) mining district, where they promote significant removal of dissolved Al (Sánchez-España et al., 2005, 2006). Other papers have addressed the role of alunite ($KAl_3(SO_4)_2(OH)_6$) on the control of Al concentration in acidified surface waters and soils (*e.g.*, Adams and Rawajfih, 1977; Nordstrom, 1982; Singh, 1982), and geochemical modelling calculations usually suggest saturation of many acid pit lakes with respect to this mineral (Eary, 1999; Sánchez-España et al., 2011; Eary and Castendyk, 2013).

A number of likely controls on Al solubility have been proposed in surface waters. Gibbsite and kaolinite solubilities usually control aluminum concentration in natural waters, and the behaviour of Al in acidic waters has traditionally been explained by the precipitation of microcrystalline gibbsite or amorphous $Al(OH)_3$ through reaction 3 (Nordstrom, 1982; Driscoll et al., 1984; Nordstrom and Ball, 1986; Hendershot et al., 1996; Nordstrom and Alpers, 1999):

$$Al^{3+}_{(aq)} + 3H_2O_{(l)} \leftrightarrow Al(OH)_{3(s)} + 3H^{+}_{(aq)} \quad (3)$$

The presence of dissolved sulfate modifies the behaviour of aluminum under acidic conditions, and the solubility of this metal is controlled by some other minerals (such as alunite or felsobanyaite) which can precipitate at lower pH with respect to near-neutral waters with little or no dissolved sulfate (Nordstrom, 1982; Bertsch and Parker, 1996; Bigham and Nordstrom, 2000). Thus, the transition between conservative (i.e., dissolved concentrations remaining constant or increasing) to reactive (i.e., decreasing dissolved concentrations) behaviour of dissolved aluminum in several pit lakes has been observed to occur at pH~4.0 (Sánchez-España et al., 2011), which is consistent with previous observations in tailings pore waters (Blowes et al., 2003) as well as in acid sulfate soils (Mosley et al., 2014a,b).

The behaviour of Al at pH<4.0 has been controversial (see discussions in Bigham and Nordstrom, 2000, Jones et al., 2011, and Sánchez-España et al., 2011). Previous studies proposed that jurbanite ($AlSO_4OH \cdot 5H_2O$) could control the solubility of Al in acid sulfate soils and solutions (*e.g.*, Van Bremen, 1973; Karathanasis et al., 1988; Zhu and Burden, 2001). This mineral has also been proposed to control the concentration of Al in pit lakes (Eary, 1999; Eary and Castendyk, 2013). However, in most occasions the possible role of jurbanite has been suggested solely by geochemical modelling, while the presence of this mineral in the studied systems has never been demonstrated. Jurbanite has only been observed as a typical efflorescent mineral (Anthony and McLean, 1976) and this mineral has probably no role on the control of Al solubility in acidic waters.

The aim of this study was to expand the current knowledge on the mobility of Al at low pH. For our research, we selected several pit lakes of the IPB in SW Spain. These artificial water bodies constitute field-scale laboratories of incomparable value, hosting highly acidic and Al-rich water over long periods of time (often decades). Furthermore, the wide compositional spectrum found in these lakes (pH=2.2-4.5, [Al]=2-20 mM, $[SO_4^{2-}]$=0.02-0.3

M) provides a suitable window for the study of aluminum solubility under typical conditions of AMD and many acidic soils and sediment pore waters. In this first paper of a two-part series, we focus on the behaviour of Al at the lowest pH range (pH<4.0) where Al precipitation is both kinetically and thermodynamically unfavourable and where this metal is often considered to behave conservatively.

With this purpose, we studied mineral colloids found at different depths (ranging from near-surface to 100 m) in the water column of the highly acidic (pH 2.2-3.1) San Telmo pit lake. To expand the pH window of our study, we also include observations and analyses obtained on schwertmannite particles and jarosite crystals formed at slightly higher pH (up to 4.3) in the nearby pit lakes of Cueva de la Mora and Herrerías. Further limnological, hydrogeochemical and microbiological information about these lakes can be found in recent studies (*e.g.*, Sánchez-España et al., 2009, 2011, 2012, 2013, 2014; Diez-Ercilla et al., 2009, 2014; Wendt-Potthoff et al., 2012; Falagán et al., 2014).

2. MATERIALS AND METHODS

2.1. Environmental framework

The San Telmo pit lake (Fig. 1) was formed by flooding of a former, large open pit which was mined until 1990 for the recovery of Cu, Zn and Pb from massive sulphide ore mineralization. The ore deposit was hosted in hydrothermally altered volcanic rocks (mainly rhyolites) associated to clastic sedimentary rocks (shales) of Carboniferous age. Today this 130 m-deep lake is meromictic and comprises an upper mixolimnion of around 29 m depth (which seasonally mixes and experiences winter overturn) and a deep monimolimnion which is perennially isolated from the atmospheric conditions. However, unlike most other meromictic pit lakes of the IPB, where Fe is solely present as Fe(II) in the deep waters, the redox potential stays relatively high (ORP~420-460 mV) even in the deep, anoxic monimolimnion (Fig. 1d), and Fe(III) is present throughout the whole water column. This is an unusual feature which makes this lake an outstanding "geochemical reactor" with more than 8 Mm^3 of Fe(III)-precipitating acidic water. The pH is strongly buffered by the precipitation of Fe(III) in the form of either schwertmannite and/or jarosite, though schwertmannite is metastable and tends to transform to jarosite and/or goethite during aging (Bigham et al., 1996; Sanchez-España et al., 2011, 2012). Seasonal fluctuations of pH throughout the year (Fig. 1e) result from the combined effects of diverse geochemical and

hydrological factors, including: (i) volume and composition of inflowing waters –mostly AMD seeping from adjacent waste piles, but also groundwater and direct meteoric precipitation–, (ii) evapo-concentration of solutes during the dry summer season, (iii) microbially catalysed oxidation of Fe(II), (iv) microbially mediated reduction of Fe(III) and SO_4^{2-}, and (v) water/rock interaction, including the dissolution of acidity-releasing (*e.g.*, pyrite) and acidity-consuming (*e.g.*, carbonate, silicate) minerals.

There is a marked increase in conductivity and sulfate concentration below the redoxcline (Sanchez-España et al., 2012). Most metals behave conservatively and show a vertical pattern of nearly constant (e.g., SiO_2, Cl) or increasing (e.g., Ca, Mg, Mn, Cu, Zn, Cd, Co, Ni) concentration with depth (Table 1; *see also Fig. EA1 in electronic annex*). In this context, both Fe(III) and Al display an opposite trend, showing clear signs of removal by precipitation and/or sorption reactions (Table 1; Fig. 2a). Furthermore, some other trace elements like K (Fig. 2b), and toxic metal(oid)s like As, Cr, Mo and Pb (Table 1; Fig. 2c-d), show a similar decreasing trend which is likely linked to the mobility of both iron and aluminium, as discussed below.

2.2. Field work and sampling

The waters and solids studied in this work were obtained during different field campaigns conducted between 2006 and 2015. We used densely coated membrane filters (0.1 and 0.45 µm pore size; Millipore®) to study the chemical and mineralogical nature of colloidal precipitates existing at different depths in the lakes. These filters were obtained by filtering 250 mL of water collected from discrete depths. The filters were washed by subsequent filtration of 50-100 mL of ultra-pure deionized water (MilliQ), stored at 4 ºC and used for mineralogical identification and chemical characterization. In addition, we also used sediment traps installed in the San Telmo pit lake at depths of 30, 40 and 100 m. These traps were sampled every 3-4 months during this time interval. All traps were attached to 6 mm-thick mooring lines anchored to the lake bottom. These PVC traps (supplied by Hydro-Bios; GmbH, Kiel-Holtenau, Germany) had a collection area of 150 cm^2, and a cylinder length of 56 cm within a 250 mL polyethylene bottle. The sediment traps collected a significant amount of chemical precipitates formed *in situ* at depth, in addition to fine-grained sediments that settled from above. Immediately after collection, these sediments were carefully washed by submersion in consecutive MilliQ water baths (without sonication or shaking), dried at room temperature and stored at ambient conditions until microscopic analysis.

Field measurements (pH, ORP, T, O_2) were taken with a Hydrolab MS5 multi-parametric probe (Hach®, Loveland, CO, USA), after calibration with fresh standards. Water samples for chemical analyses were taken from different depths with a Van Dorn® sampling bottle (KC Denmark). All samples were filtered on site with 0.45 µm nitrocellulose membrane filters (Millipore®), stored in 125 mL-polyethylene bottles, acidified with HNO_3 (1 M), and preserved on ice in coolers during transport.

2.3. Laboratory analyses of waters

Water samples were analyzed by atomic absorption spectrometry (AAS; major cations), inductively coupled plasma-atomic emission spectrometry (ICP-AES; S as SO_4^{2-}), and inductively coupled plasma-mass spectrometry (ICP-MS; trace metals) using Varian SpectrAA 220 FS, Varian Vista MPX and Agilent 7500ce instruments, respectively. For simplification, only some of these elements will be discussed in this work. The detection limit for major cations was <1 mg/L. The detection limits for trace elements was usually between 0.4 µg/L (e.g., As) to 10 µg/L (e.g., Pb).

2.4. Chemical and mineralogical identification of bulk Fe(III)-Al precipitates

The aluminous and ferric precipitates were initially characterized by inductively coupled plasma atomic emission spectroscopy (ICP-AES) after previous acid digestion with HF, $HClO_4$, HNO_3, and HCl for the determination of major cations (Al, Fe) and trace metal(oid)s (including As, Pb, Cu and Zn). These solids were also mineralogically identified by powder XRD on a PANalytical X'Pert Pro diffractometer (X'Pert software with ICDD database), with Cu Kα radiation (40 kV, 40 mA), graphite monochromator and automatic slit.Cryogenic ^{57}Fe transmission Mössbauer spectroscopy was also carried out on selected ferric precipitates from the San Telmo pit lake at a temperature of 5 K. Solid material was scraped off filter paper and sealed between two pieces of 5 Mil Kapton tape and mounted on the sample holder. The ^{57}Co radioactive source (~50 mC_i) resided in an R_h-matrix at room temperature during data collection. Spectral fitting was done using Recoil software (University of Ottawa, Canada) using the Voigt-based model (Rancourt and Ping, 1991). Data were calibrated against an α-^{57}Fe foil collected at room temperature.

2.5. Scanning and transmission electron microscopy characterization of Fe(III)-Al particles/crystals

198 The aluminous and ferric precipitates naturally formed in the lakes were initially studied
199 by scanning electron microscopy (SEM) coupled with an energy-dispersive X-ray
200 spectrometer (EDS), and transmission electron microscopy (TEM) equipped with EDS. These
201 studies were conducted at the SGIker Advanced Research Facilities (UPV/EHU).
202 Compositional analyses were carried out on carbon-coated samples by EDS on a JSM-7000F
203 field emission scanning electron microscope (JEOL) working at 20 kV. These analyses
204 provided valuable information of mineral chemistry on a sub-micron analyses volume. Among
205 hundreds of analyses conducted in the precipitates from the lakes, we only considered those
206 showing no evidence of fine-grained detrital silicate contamination. TEM images and selected
207 area electron diffraction (SAED) analyses of Fe(III) and Al compounds were performed on a
208 Philips CM200 transmission electron microscope after placing 2-3 drops of an ethanol
209 suspension with the fine precipitates on a porous carbon film supported by a Cu grid.

210 Ultra high-resolution imaging and compositional analysis was performed using a double
211 aberration-corrected FEI Titan^3 G2 60-300 scanning/transmission electron microscope
212 (S/TEM) at the Materials Characterization Laboratory (MCL) of the Materials Research
213 Institute (MRI) in The Pennsylvania State University. This microscope has sub-Ångstrom
214 resolution and can be used to determine both crystal structure and elemental composition over
215 large areas of the sample. EDS maps were acquired using FEI's ChemiSTEM technology,
216 which combines a high brightness Schottky field emission gun with four Super-X silicon drift
217 x-ray detectors. This EDS system produces very high x-ray count rates, which allowed
218 crystals to be compositionally mapped at an average time of 5 minutes per map and a beam
219 current of approximately 0.7 nA. Samples were sonicated in an ethanol bath and then placed
220 on lacey carbon-coated Cu grids before being inserted into the microscope. The samples were
221 studied using both 80 and 200 kV for HAADF (high angle annular dark field) STEM, which
222 provides high resolution images containing primarily mass contrast, and EDS elemental
223 mapping of crystals and particles with diameters comprised between 200 nm and 1 μm. EDS
224 mapping at low magnification (e.g., 5,000×), either displayed independently or combined with
225 the HAADF-STEM image, is useful for rapid identification of minerals over a relatively large
226 selected area. Further analyses of selected crystals at higher magnification (up to 80,000×)
227 permitted a more thorough investigation of Al and Fe(III) distribution via detailed crystal EDS
228 mapping and transversal (through-crystal) EDS line scans. The spectra obtained by EDS
229 analysis was quantified by the Cliff-Lorimer ratio method to obtain the relative concentrations

between the elements from the EDS peak intensities after perfoming a background subtraction and peak deconvolution using the Bruker Espirit software.

We also obtained structural information on selected alunite and jarosite crystals by high resolution transmission electron microscopy (HRTEM), including d-spacings measured on the HRTEM images and/or between diffraction spots and rings in the SAED patterns.

EDS has long been used in geology to aid in the microscopic study of minerals and compounds (Friel et al., 2003; Garratt-Reed and Bell, 2003, and references therein) and recently has greatly improved the performance and reliability for chemical characterization of materials after the incorporation of silicon drift detectors to the modern scanning and transmission electron microscopes (Newbury and Ritchie, 2013a,b). Our analyses were calibrated with different minerals of known mineralogy which were used as internal standards. We then compared the results (after adequate peak verification and background correction) to the corresponding ideal compositions. A selection of "pure specimen" analyses (conducted on minerals almost free of trace elements) is provided in the supplemental material (*Table EA1*). In general, a close similarity was found for the EDS analyses of pure schwertmannite, K-jarosite, H_3O-jarosite, hydrobasaluminite, alunite and gypsum crystals with respect to their ideal compositions, as well as with analyses previously obtained by other techniques. The variability in the concentration of elements like Al, Fe, K, O and S in jarosites and alunites were thus considered natural chemical trends resulting from K^+/H_3O^+ or Fe/Al substitution. The K^+/H_3O^+ molar ratio of the analysed jarosites and alunites was calculated from the EDS analyses based on the theoretical stoichiometry (one mol of alkalies per formula unit) and inferring the hydronium content as $[H_3O^+]=(1-K^+-Na^+)$. Taking into account the small size of these precipitates (usually below 1 µm), STEM-EDS analyses provide the most reliable compositions and better define the chemistry of the whole crystal.

2.6. Water/mineral equilibrium calculations

We used PHREEQC (Version 3.0.5-7748; Parkhurst and Appelo, 2013) to calculate the saturation index (SI) of Fe(III) and Al minerals, including alunite, gibbsite, goethite, H_3O-jarosite, K-jarosite, and schwertmannite, in the pit lake waters. All calculations were made using the WATEQ4F thermodynamic database (Ball and Nordstrom, 1991), previously modified with solubility product constants for K^+- and H_3O^+-jarosite end-members (taken from Alpers et al., 1989 and Baron and Palmer, 1996) and schwertmannite (taken from

Bigham et al., 1996). For these calculations, we considered physico-chemical parameters measured on site (pH, ORP, T, O_2) and included all the cationic and anionic species in solution. Ionic activities were calculated with the Davies equation (Davies, 1962). The ionic strength of the analyzed waters was around 0.1-0.2 molar. The pressure gradient across the water column (1-10 bar) is small in absolute terms, and its effect on water/mineral equilibrium was not considered in the calculations. We did consider, however, the variation of water density between different depths, as this parameter affects the molal proportions calculated from solute concentrations introduced as mg L^{-1} or µg L^{-1}. Water density was calculated based on temperature and solute concentration using the RHOMV 2.0 numerical program (Boehrer et al., 2010; available at www.ufz.de).

3. RESULTS

3.1. General chemical and microscopic features

Based on XRD, mineral precipitates found in the deep (i.e., >35 m) anoxic waters of the San Telmo acid pit lake (pH<3.2) were dominated by jarosite along with trace amounts of schwertmannite and quartz. The predominance of Fe(III) [and absence of Fe(II)] in these minerals was confirmed by Mössbauer spectroscopy (*Fig. EA3 in electronic annex*). Even though the sample contained trace schwertmannite, the Mössbauer spectra were well fit to a reference jarosite spectrum, consistent with XRD results (not shown). Whole-sample chemical analyses carried out by ICP-AES on these solids yielded total iron concentrations in the range of 25.9-27.4 wt.% Fe which are lower than theoretical values of ideal K- or H_3O-jarosite (33.9-35.5 wt.%) (*Table EA2 in electronic annex*). These precipitates also contained significant Al (3.9-4.3 wt.%) in addition to trace components such as As, Pb, Cu and Zn at concentrations commonly exceeding 1,000 mg/kg (*Table EA2*). Detailed SEM and STEM studies have revealed that these trace constituents were incorporated into both jarosite and schwertmannite through adsorption and/or ionic substitution, as discussed below.

The microscopic examination of these particles by SEM and TEM also showed a mineral assemblage dominated by jarosite and coexisting schwertmannite at all depths, though subordinate alunite was also observed (Fig. 3). Schwertmannite displays a typical *hedge-hog* morphology with nanometric whiskers that grew radially and formed pseudo-spherical aggregates (Fig. 3a), while jarosite and alunite were usually present as idiomorphic crystals with pseudo-cubic to rhombic habit and diameters ranging from 200 nm to 1 µm. Some

jarosite crystals displayed a clear concentric zoning which indicates chemical heterogeneity during successive stages of crystal growth (Fig. 3c-d). Textural and compositional features of these coexisting minerals suggest that many jarosite crystals actually resulted by transformation of previously formed schwertmannite, though direct precipitation of jarosite from the parent fluid also takes place at pH<2.5 (Sanchez-España et al., 2012).

Jarosite crystals often showed an important potassium deficit suggestive of hydronium substitution (Fig. 3a-b), which has led to their classification as hydronian (H_3O-) jarosites (Sánchez-España et al., 2012). Further, SEM spot-size EDS analyses conducted on selected areas of schwertmannite particles and jarosite crystals indicated that these two minerals may contain significant amounts of adsorbed and/or coprecipitated elements such as Al, Mg and Si (Fig. 3a-b). Most notably, the variable and locally high concentration of Al found in schwertmannite and jarosite was also indicative of an important degree of Fe(III)-Al co-precipitation by either Al adsorption (likely dominant in schwertmannite) and/or Al/Fe substitution (prevailing in jarosite). To confirm this possibility, we used STEM to conduct spatially-resolved, whole-crystal elemental mapping in schwertmannite particles and jarosite crystals.

3.2. Schwertmannite chemistry

The STEM-EDS images obtained for schwertmannite particles formed in the studied pit lakes (San Telmo, Cueva de la Mora and Herrerías) revealed a variable distribution of Al. Some aggregates showed a homogenous distribution of Al throughout the particles, nearly identical to that of major components such as Fe and S (Fig. 4).

In any case, the concentration of Al in schwertmannite was variable and seemed to be pH-dependent (Table 2; Fig. 5). Among the chemically homogenous schwertmannite particles, those found at higher pH (~4.0) had higher Al content (2.56-3.37 at.%, Fe/[Fe+Al]=0.89-0.90), while those formed at lower pH (2.6-3.5) showed lower Al content (Al<1.2 at.%, Fe/[Fe+Al]=0.95-1.00).

At higher pH (>4.0), Al tended to be more heterogeneously distributed and chemical partitioning was clearly visible, suggesting a distinct mechanism of entrapment. Nano-scale elemental mapping and chemical through-particle scanning of schwertmannite particles found in the deep part of the Herrerías pit lake (pH 4.3) showed Al to be especially concentrated in outer areas adjacent to the needles (Fig. 6). The example illustrated in Fig. 6 (*see also Fig.*

EA4 in electronic annex) shows the strong chemical contrast between the core and needles in schwertmannite particles with typical *pincushion* morphology. Even though Al was always present in the inner zones at significant concentrations (*e.g.*, 8.2-8.4 at.%), Al was far more abundant in outer zones (*e.g.*, 15.8-17.1 at.% Al) (Table 2; Fig. 6b), where it seemed to surround the whiskers (Fig. 6c-d).

While the inner zones (with Fe/S=6.2-6.5 and Fe/[Fe+Al]=0.77-0.79) may still represent a non-ideal schwertmannite with a higher degree of Al/Fe substitution due to a higher pH, the outer zones have a very distinct composition (with Fe/S=2.6-2.8 and Fe/[Fe+Al]=0.41-0.48) and more likely represent an Al shell formed by adsorption on pre-existing schwertmannite (Table 2; Fig. 5a).

Geochemical modelling suggests that, within the pH range of most acidic mine waters (2.0-4.5), dissolved Al is mostly present as $AlSO_4^+$ and $Al(SO_4)_2^-$ complexes, along with minor Al^{3+} (Fig. 5b; Sanchez-España, 2007). An important inflection point exists around pH 3.3 and marks the dominance of the cationic $AlSO_4^+$ (dominant at pH<3.3) versus the anionic $Al(SO_4)_2^-$ (dominant at pH>3.3).

3.3. Jarosite and alunite chemistry

The presence of relatively pure Al minerals (e.g., alunite, gibbsite) could not be detected by XRD. However, the use of chemical mapping with STEM allowed us to identify both jarosite and alunite nanocrystals, and to measure the distribution of Fe and Al in these crystals (Figs. 7-9; *see also Figs. EA5 and EA6 in the electronic annex*).

Chemical mapping of Fe(III) and Al showed that nearly pure (end-member) jarosite could coexist with both end-member alunite and concentrically zoned Al-Fe crystals. These crystals were found to be composed of a jarositic rim (250-400 nm thickness) surrounding an Al-rich core with composition intermediate between alunite and jarosite (Figs. 7-8). In some of these zoned crystals, the Al content decreased progressively from the crystal center to the outer rims, suggesting a replacement process defined by the isomorphic transformation/substitution of previously formed alunite to more stable jarosite during ageing (Fig. 7). In other cases, however, the trends of Fe(III) and Al distribution within the crystals were not progressive and more likely reflected distinct stages of crystal growth (Fig. 8). Such distinct stages could have occurred during slightly varying geochemical conditions (e.g., pH) in the parent solution, in

accordance with previous findings in other jarosite growth zonings described in the literature (e.g., Papike et al., 2006; Burger et al., 2009).

Chemically homogeneous crystals of nearly pure alunite with very low content of Fe(III) were also observed in these samples (Fig. 9), though they were far less abundant than jarosite at all depths, consistent with the inability to detect alunite by XRD.

Electron diffraction and high resolution images of selected areas of these crystals helped confirm the mineralogical nature of these two phases (Fig. 10). Although we could not obtain the full set of diagnostic d-spacings, many of the Fe-rich crystals yielded d-spacings matching with those of K-jarosite and/or H_3O-jarosite (*e.g.*, Fig. 10a). In the case of alunite, the diffractometric identification was less clear since the crystals apparently displayed a slightly lower crystallinity with lesser rings and spots. However, we could find a few d-spacings corresponding to alunite in the Al-rich crystals (*e.g.*, Fig. 10b).

Chemical quantification of both chemically homogeneous and concentrically zoned crystals of jarosite and alunite indicated highly variable concentrations of Al and Fe ($Fe/[Fe+Al]_m$=0.54-0.99 in jarosites and $Fe/[Fe+Al]_m$=0.07-0.37 in alunites; Table 3, Fig. 11; *see also Table EA3 in electronic annex*). The potassium content was also highly variable ($H_3O^+/[H_3O^+ + K^+]_m$=0.01-0.86 in jarosites, and $H_3O^+/[H_3O^+ + K^+]_m$=0.01-0.55 in alunites) and indicated variable H_3O^+/K^+ substitution in both minerals.

Saturation index (SI) calculations for a number of Fe(III) and pure Al phases in the San Telmo pit lake help explain the equilibrium conditions of jarosite and alunite stability (Figs. 12-13). The evolution of SI with depth is shown in Fig. 12, while the evolution of these indices with pH is provided in Fig. 13a. The plots of Fig. 12 reflect two different scenarios which illustrate the situation at the beginning of summer (June 2006, pH=2.4-2.6; Fig. 12a) and at the beginning of spring (April 2011; pH=2.8-3.0; Fig. 12b). In April 2011, the mixolimnetic waters were strongly oversaturated with respect to schwertmannite, and this mineral is commonly the first and most abundant product of Fe^{III} precipitation in the lake. Below the redoxcline, however, schwertmannite is no longer stable (SI<0) and tends to transform to jarosite and/or goethite (Sanchez-España et al., 2012). The low pH of the lake favours the substitution of H_3O^+ for K^+ in the alkali site and the formation of hydronian jarosite, which is common in very acidic systems (*e.g.*, Alpers et al., 1989; Dutrizac and Jambor, 2000; Stoffregen et al., 2000; Jamieson et al., 2005). On the other hand, Al minerals

(exemplified here by alunite and gibbsite) are notably undersaturated at all depths and in the two periods studied (Fig. 12), consistent with the relative scarcity of alunite and the absence of gibbsite. However, the finding of alunite crystals indicates that this mineral was likely formed under slightly different geochemical conditions (*e.g.*, higher pH) with respect to those measured in the parent fluid at the moment of sampling.

The calculated saturation indices plotted against pH help define pH limits and stability fields for the studied minerals (Fig. 13a). This plot indicates precipitation of schwertmannite at pH>2.5, and precipitation of H_3O-jarosite at pH>2.4 for the geochemical conditions found in the San Telmo pit lake. K-jarosite is oversaturated in every case and its precipitation is therefore feasible in the whole pH window (2.0-3.5). Alunite is always undersaturated, as already stated, and extrapolation of the available data indicate that it could precipitate at a pH around 3.3 (Fig. 13a). This pH is only slightly higher than the highest pH value measured in the San Telmo pit lake (3.1) and may well have existed at certain periods or in restricted micro-environments such as in the surroundings of microbial cells.

The pH limits obtained in Fig. 13a allowed us to establish a geochemical model for the Fe(III)-Al system with stability fields for the most relevant Fe(III) and Al minerals formed in AMD systems (Fig. 13b). We have considered the electronic potential (pe) to discriminate between Fe(II)- and Fe(III)-dominated systems, as the presence of Fe(III) may strongly influence the behaviour of dissolved Al at low pH. We selected a limit of pe~6.7 (Eh~400 mV) to separate both fields based on previous studies (*e.g.*, Sanchez-España et al., 2005; Diez-Ercilla et al., 2014). We have also enlarged the pH window to pH 7 to include phases stable under more neutral conditions. The diagram was produced considering the Fe-Al-K-S-O-H system for relatively dilute conditions ($a_{SO4}=10^{-2}$-10^{-1}, $a_{Fe}=a_{Al}=10^{-3}$, $a_K=10^{-5}$). Therefore, phases forming in more concentrated solutions (*e.g.*, evaporative brines), such as alunogen, or phases incorporating other cations (*e.g.*, natro-jarosite) were not considered.

4. DISCUSSION

4.1. Incorporation of Al into schwertmannite

It is well known that Al^{3+} can substitute isomorphously for Fe^{3+} in iron oxides, and may occupy up to a third of the structural sites of Fe^{3+} in minerals such as goethite (Cornell and Schwertmann, 2003). Although schwertmannite is a well-known adsorbent for many toxic trace elements, including As and Cr (*e.g.*, Regenspurg and Peiffer, 2005; Sanchez-España et

al., 2005, 2006; Burton et al., 2009), the extent and mechanisms of Al incorporation into this mineral have not been studied in detail.

The homogeneous distribution of Al throughout many schwertmannite particles (Fig. 4d) points to a likely incorporation of Al into schwertmannite, either by adsorption and/or through inclusion and later entrapment during precipitation and subsequent mineral growth. The adsorption of Al on schwertmannite is supported by the geochemical environment in which the schwertmannite particles were found. The monimolimnion in the Herrerías pit lake is anoxic and lacks any Fe(III) in solution, so that the schwertmannite particles were probably formed in the upper, oxidizing layer and were subsequently transported downwards by settling. The interaction of Al ionic complexes in solution with the schwertmannite particles during settling probably led to this strong Al adsorption on the high surface area whiskers. This adsorption may have been favoured by the electrostatic attraction between the positively charged surfaces of schwertmannite particles (with pH_{ZPC}=6.6-7.1; Regenspurg, 2002) and negatively charged species like $Al(SO_4)_2^-$. The feasibility for Al sorption onto pre-existing Fe(III) phases in the pH range covered in this study is supported by geochemical modelling (Fig. 5b). In contrast, very limited or negligible Al sorption should be expected at pH<2.5 (either for absence of suitable Fe(III) adsorbent phase or due to dominance of Al^{3+} and $AlSO_4^+$ species) and at pH>4.5 (where Al removal will occur chiefly by precipitation as Al-oxyhydroxysulfate and/or Al-hydroxide minerals).

The kinetics of Al sorption and incorporation into schwertmannite is unknown, but the long residence time of the deep waters in these lakes and the slow settling velocity of the fine-grained schwertmannite particles are both hydraulic factors that should enhance adsorption.

The possibility of structural substitution of Al^{3+} for Fe^{3+} cannot be ruled out, though the existence of Al-substituted schwertmannites cannot be demonstrated in the present work. This question will require further in-depth nano-structural and crystallographic studies.

4.2. The jarosite-alunite solid solution

The inverse correlation between Fe and Al concentration in the analysed jarosite and alunite crystals likely reflects Fe/Al substitution and a solid solution series between the two end-members (Fig. 11a). Considering only the data set from San Telmo (R^2=0.97), the Fe-Al analytical trend parallels the ideal solid solution trend. Additional data from other pit lakes (Cueva de la Mora, Herrerías) introduce some scatter, but do not reveal a bimodal distribution.

446 However, when considering atomic proportions plotted in a binary diagram of $Fe/[Fe+Al]_m$ *vs.*
447 $H_3O^+/[H_3O^+ + K^+]_m$, it seems that two populations do exist (Fig. 11b). The analytical points can
448 be grouped into either Fe-rich alunites or Al-rich, hydronian jarosites, with few points lying in
449 between. This plot reveals a double solid solution series where Fe^{3+}/Al^{3+} substitution and
450 K^+/H_3O^+ substitution are coupled and where the hydronian substitution in the jarosites is
451 notably more important than in alunites. It is difficult to ascertain whether the scarcity of
452 intermediate points reflects a crystallographically controlled miscibility gap or simply reflects
453 the very singular geochemical conditions enabling the formation of transitional compositions
454 with nearly equivalent molar proportions of Fe and Al. The existence of a few intermediate
455 compositions may suggest that these compositions are structurally feasible but waters with
456 comparable concentrations of Al and Fe(III) are an underrepresented geochemical condition
457 required for their formation.

458 The complete solid solution between alunite and jarosite has been experimentally
459 synthesized in the laboratory (Brophy et al., 1962; Härtig et al., 1984), however the
460 occurrence of this solid solution has rarely been found in nature (Brophy et al., 1962; Alpers et
461 al., 1989, 1992). Compositions intermediate between jarosite and alunite end members (i.e.,
462 those with comparable molar proportions of Fe and Al in the octahedral (B) site) are very
463 uncommon in the literature, which has led some authors hypothesize about the possible
464 existence of a miscibility gap in this solid solution. It has been argued that such a miscibility
465 gap is unlikely (*e.g.*, see discussions in Alpers et al., 1989, Stoffregen et al., 2000, Dutrizac
466 and Jambor, 2000, or Papike et al., 2006), so that the apparent scarcity of intermediate
467 compositions would be more likely a result of the physical separation of Fe^{3+} from Al^{3+} in
468 natural waters due to their very different first hydrolysis constants (pK_1 Fe^{3+}=2.19, pK_1
469 Al^{3+}=4.99; Nordstrom and Ball, 1986). Alunite formation seems to be enhanced in
470 environments where ferric iron is absent or not abundant (Keith et al., 1979; Alpers et al.,
471 1989). The results obtained in this study suggest that both alunite and jarosite may form and
472 coexist in the same aqueous environment, provided that suitable geochemical conditions are
473 met. These conditions ideally include comparable molar concentrations of Al and Fe(III), and
474 a pH window enabling the formation of both minerals (see discussion below). The formation
475 of Fe(III)-containing alunite and Al-rich jarosite in the monimolimnion of the San Telmo pit
476 lake appears to be enhanced by several factors, most notably the higher molar concentration of
477 aluminum with respect to that of ferric iron (5-7 mM Al^{3+} vs. 2-3 mM Fe^{III}; Fig. 2a). If it

exists, the compositional gap in this solid solution is probably significantly smaller than what has been traditionally considered.

Furthermore, the presence of isolated Fe-containing alunite crystals not associated with schwertmannite suggests that these solids have directly precipitated from the parent solution by incorporation of Al^{3+} for Fe^{3+} into the mineral structure during crystallization. The zoned crystals with distinct alunite and jarosite domains likely reflect the metastability of the former with respect to the later, so that many analyses in the plots of Fig. 11 may well reflect different stages of an alunite to jarosite isomorphic replacement with different degrees of completion.

Although the hydronium substitution was always much more important in jarosite, it is worth to note that we have also identified an important presence of H_3O^+ in the alkali site in alunites. This H_3O^+/K^+ substitution has been rarely demonstrated in nature, but has been inferred in both synthetic and low-temperature natural alunites because of a deficiency in alkalis and an excess of water compared with the stoichiometric composition (e.g., Ripmeester et al., 1986; Stoffregen et al., 2000).

The analyzed jarosites and alunites could also incorporate small quantities of Si and Mg (0.4-6% Si; 0.5-2.6% Mg; *see Table EA3 in electronic annex*), though these two elements are considered to be adsorbed rather than structural. Silicon is included in the formula of some rare minerals of the alunite supergroup (*e.g.*, waylandite, eylettersite), but the formation of these minerals requires the presence of SiO_4^{4+} which is only possible under highly basic conditions. Under acidic conditions, analytically determined silicon is most likely present as adsorbed complex anions or as amorphous silica gels and not as solid-solution Si (Dutrizac and Jambor, 2000).

4.3. Water/mineral equilibrium

According to the diagram of Fig. 13b, alunite would be only stable over a narrow window of pH (3.3-4.0). Above pH 4.0, the precipitation of hydrobasaluminite and/or felsobänyaite would be kinetically favoured (Sanchez-España et al., 2011) and these minerals would be the main Al sink up to a pH around 6.0. Above pH 6.0, Al-OH complexes become more abundant than Al-SO_4 complexes (Fig. 5b; Sanchez-España, 2007) and gibbsite formation is favoured. The formation of gibbsite and hydrobasaluminite has been observed in the studied lakes with pH>4.0, and will be presented in another study.

Below pH 3.3, the behaviour of Al is strongly dependent on redox potential. At pe>6.7, the presence of Fe(III) enhances the formation of different phases, depending on pH conditions. K-jarosite is stable above pH 2.0, while schwertmannite is both kinetically and thermodynamically favoured at pH>2.5-2.6 (Fig. 13a-b). The stability field of hydronian jarosite is limited by its apparent instability below pH 2.3 and the aforementioned faster kinetics of schwertmannite precipitation above pH 2.5. Under reducing conditions with low redox potential, however, the absence of Fe(III) solids to adsorb and/or entrap Al would lead this metal to stay in solution in different ionic forms ($AlSO_4^+$, $Al(SO_4)_2^-$, Al^{3+}) at pH<3.3. Above this pH limit, however, a limited amount of Al-Fe co-precipitation would still be possible through variable adsorption of Fe(II) ions onto the formed Al phases.

This conceptual figure is consistent with stability diagrams proposed separately for the Fe(III) and Al systems in previous studies (e.g., Nordstrom, 1982; Bigham et al., 1996; Bigham and Nordstrom, 2000), and provides a reliable model to account for the behaviour of Al at low pH. Most notably, it links the mobility of dissolved Al at pH<3.3 with its interaction with coexisting Fe(III) phases, and not with discrete Al precipitation in the form of Al phases such as jurbanite, which has been shown to be irrelevant as a solubility control of Al in acidic mine waters (Bigham and Nordstrom, 2000; Jones et al., 2011; Sanchez-España et al., 2011). The incorporation of Al into the Fe(III) phases would be strongly pH-dependent, with negligible incorporation at very low pH (i.e., pH<2.0) and increasing Al uptake with increasing pH (Figs. 5a and 13b).

In geochemically varying systems such as these acid pit lakes (pH window of 2.2-4.3 resulting from spatial and temporal variation) the presented geochemical model predicts the possible coexistence of several mineral sinks of Al, including Al-containing jarosite, Al-adsorbed schwertmannite, alunite, and hydrobasaluminite. This is valid for environmental aqueous solutions, as the meta-stability of some of these phases (e.g., schwertmannite with respect to jarosite and/or goethite, hydrobasaluminite with respect to alunite) will theoretically tend to significantly reduce this diversity of Al sinks to only one or two stable minerals in the bottom sediments of the lakes.

4.4. Overall effects of Al-Fe(III) co-precipitation on metal mobility

The combined effects of schwertmannite and jarosite-alunite precipitation on the water chemistry of the San Temo pit lake are illustrated in Fig. 2. In these vertical profiles of

element concentrations, the surface water is variably influenced by seasonal changes (both in composition and volume) of acid mine drainage inflow seeping from nearby waste piles. The following observations on metal mobility refer to depths below 10 m depth, where the water chemistry is mostly controlled by internal hydrogeochemical and geomicrobial processes occurring in the lake, rather than by external factors.

Within a general context of conservative behaviour for most metals (which tend to increase their concentrations with depth; *see Fig. EA1 in electronic annex*), total iron (Fe_T), Al, As and Pb are significantly decreased in concentration as a result of their incorporation on ferric and aluminous phases. The combination of Al-rich jarosite and schwertmannite with subordinate alunite precipitation promotes a significant decrease of dissolved Al concentration. Interestingly, the observed removal of aluminum (6-6.7 mM at 25 m depth compared to 4.7-5.3 mM at a depth of 90 m, representing a 20% net reduction) takes place in a water column where pH is usually below 3.1 (Fig. 1) and apparently without participation of any other removal mechanism such as dilution or bioaccumulation. This is noteworthy since Al is normally considered to be conservative below pH 5.0 in most surface waters.

Jarosite and alunite precipitation aids in the removal of total iron (in combination with schwertmannite; 3.5 mM above the redoxcline *vs.* 2.5 mM at depth; Fig. 2a). Other elements which also followed a decreasing vertical trend were arsenic and lead, as well as chromium and molybdenum to a minor extent (Fig. 2c-d). Schwertmannite normally contains high As and Pb (up to 3 wt.% As in the Herrerías pit lake; *not shown*). Nevertheless, arsenic has also been detected in jarosite crystals at trace concentrations by SEM-EDS and STEM-EDS (*Fig. EA7 in electronic annex*), in addition to variable contents of Pb, Cu and Zn which were very close to the detection limit and could not be precisely quantified. The uptake of As, Pb, Cu and Zn by jarosite is supported by ICP-AES analyses of bulk precipitates found at different depths in ST which were mostly composed of Al-containing jarosite (*Table EA2 in electronic annex*). The incorporation of As, Pb, Cu and Zn into the crystalline structure of jarosite can be significant, having important environmental and hydrometallurgical implications (Dutrizac and Jambor, 2000; Stoffregen et al., 2000; Forray et al., 2014). We could not find conclusive evidence for the presence of Cr or Mo in jarosite, alunite or schwertmannite, probably due to the very low concentrations of these two elements in the parent solutions and resulting solids.

5. CONCLUSIONS

570 The results presented in this study suggest that the behaviour of Al at low pH (<4.0) can
571 be largely influenced by adsorption on and/or coprecipitation with Fe(III) minerals like
572 schwertmannite and jarosite. Under conditions typical of AMD and many acid soils and
573 sediments, alunite formation is feasible and may occur at around pH>3.3, as suggested by
574 mineralogical observations and geochemical modelling. However, below this pH, and contrary
575 to the extended assumption, Al is not truly conservative, and in the presence of ferric iron,
576 both metals may co-precipitate to a substantial extent to form either particles of Al-rich
577 schwertmannite (containing up to ca. 8 at.% Al with [Fe/(Fe+Al)]=0.77) and/or crystals of
578 H_3O^+- to K^+-jarosite (containing up to ca. 10 at.% Al with [Fe/(Fe+Al)]=0.54). This Al
579 incorporation is thought to take place via adsorption on mineral surfaces in schwertmannite
580 and atomic substitution for Fe^{3+} in jarosite. Although macroscopically invisible, the amount of
581 Al bound to the Fe(III) solid phases may be important enough as to imply a significant Al
582 removal from the parent solution even at low pH values far below the first hydrolysis point of
583 this cation (pK_1=4.99). This is especially important in systems with long residence times
584 favouring metal ion-mineral interaction, such as many pit lakes, flooded mines, tailings or
585 AMD-affected aquifers.

586 Taken as a whole, the compositional pattern of the analyzed jarosites and alunites
587 suggests a discontinuous, coupled (Al^{3+}-Fe^{3+}, H_3O^+-K^+) solid solution with an apparent
588 compositional gap. The lack of intermediate compositions seems to be more closely related to
589 geochemical restrictions imposed on the precipitation of Fe(III) and Al at equivalent molar
590 proportions more than with a true immiscibility between the two end-members resulting from
591 structural limitations in the crystal lattice. It is also envisaged that alunite is unstable with
592 respect to jarosite at very low pH (<3.3), so that the stability field of this mineral only spans a
593 narrow pH range (3.3-4.0). Therefore, slight pH shifts taking place in the lakes may lead to
594 isomorphic replacement of the former mineral by the latter, which may in turn drive the
595 formation of chemically zoned crystals with jarositic rims around previously formed alunite
596 cores. The higher degree of H_3O^+-K^+ substitution in jarosites with respect to alunites would be
597 a natural consequence of the jarosite formation at a substantially lower pH as compared to
598 alunite.

599 In addition to Al, the Fe(III) solids may also incorporate significant amounts of As and
600 Pb, so that the co-precipitation of Al and Fe(III) can also exert some control on the fate and
601 transport of these toxic elements.

602 This work shows that STEM analyses capable of providing chemical information at a
603 nano-metric resolution can reveal geochemical, mineralogical and water/mineral equilibrium
604 trends which are often virtually impossible to detect by most other techniques conducted on
605 bulk samples.

606 **ACKNOWLEDGEMENTS**

607 This study was funded by different institutions, including the former Spanish Ministry of
608 Science and Innovation–MICINN through research project number CGL2009-09070, the
609 Spanish Ministry of Education, Culture and Sports (*Subprograma Estatal de Movilidad, Plan*
610 *Estatal de Investigación Científica y Técnica y de Innovación 2013-2016*), the American
611 Council for International Exchange of Scholars (CIES, US Department of State) through a
612 Fulbright visiting scholar fellowship to JSE, the Pennsylvania State University (PSIEE,
613 Department of Civil and Environmental Engineering, and Materials Research Institute) and
614 Gobierno Vasco (Grupo Invest. IT-762-13). We thank Jesús Reyes for handling the chemical
615 analyses of waters at IGME laboratories, and personnel at the SGIker facilities of the Basque
616 Country University (Ana Martínez and Sergio Fernández) and at the Materials
617 Characterization Laboratory (MCL) of the Materials Research Institute (MRI) in PSU (Key
618 Wang), for their technical support during scanning and transmission electron microscopy
619 studies. We are also grateful to Sarah Cronk and Chris Gorski from the Department of Civil
620 and Environmental Engineering at PSU for the Mossbauer spectra on Fe(III)-Al solids. This
621 manuscript has substantially benefitted from constructive comments by three anonymous
622 reviewers on an earlier version.

623 **APPENDIX A. ELECTRONIC ANNEX**

624 Supplementary data associated with this article (including analytical data, depth profiles of
625 metal concentrations, element mapping and additional STEM images of solid phases) can be
626 found in the online version of this manuscript.

627

628 **REFERENCES**

629 Adams F. and Rawajfih Z. (1977) Basaluminite and alunite: a possible cause of sulfate retention by acid soils.
630 *Soil. Sci. Soc. Am. J.* **41**, 686-692.

631 Allison J.D., Brown D.S. and Novo-Gradac J. (1999) MINTEQA2/PRODEAFA2, A geochemical assessment
632 model for environmental systems: User manual supplement for version 4.0. U.S. EPA, NERL, Athens,
633 Georgia, 42 pp.

634 Anthony J. W. and McLean W. J. (1976) Jurbanite, a new post-mine aluminum sulfate mineral from San Manuel,
635 Arizona. *Am. Mineral.* **61**, 1-4.

636 Alpers C.N., Nordstrom D.K. and Ball J.W. (1989) Solubility of jarosite solid solutions precipitated from acid
637 mine waters, iron Mountain, califronia, USA. *Sci. Géol. Bull.* **42-4**, 281-298.

638 Alpers C.N., Rye R.R., Nordstrom D.K., White L.D. and King B.S. (1992) Chemical, crystallographic and stable
639 isotopic properties of alunite and jarosite from acid-hypersaline Australian lakes. *Chemical Geology* **96**, 203-
640 226.

641 Ball J.W. and Nordstrom, D.K. (1991) User's manual for wateq4f, with revised thermodynamic data, base and
642 test cases for calculating speciation of major, trace, and redox elements in natural waters. USGS Open-File
643 Report 91-183.

644 Baron D. and Palmer C. (1996) Solubility of jarosite at 4-35°C. *Geochimica et Cosmochimica Acta* **60- 2**, 185-
645 195.

646 Bertsch P.M. and Parker B.R. (1996) Aqueous polynuclear aluminum species. In: Sposito G. (Ed.), The
647 Environmental Chemistry of Aluminum, 2nd ed., Lewis Publishers-CRC Press LLC, Boca Raton, Florida, pp
648 117-168.

649 Bigham J.M. and Nordstrom D.K. (2000) Iron and Aluminum Hydroxysulfates from Acid Sulfate Waters. In
650 Sulfate Minerals: Crystallography, Geochemistry, and Environmental Significance (Alpers, C.N., Jambor,
651 J.L., Nordstrom, D.K., Eds.). *Reviews in Mineralogy & Geochemistry* **40**, 351-403.

652 Blowes D.W., Ptacek C.J. and Jourjovec, J. (2003) Mill tailings: Hydrogeology and Geochemistry. In Jambor
653 J.L., Blowes D.W. and Ritchie A.I.M. (Eds.) *Environmental Aspects of Mine Wastes*, Mineralogical
654 Association of Canada, Short Course Series 31, Vancouver, British Columbia, 2003, 95-116.

655 Boehrer B., Herzsprung P., Schultze M. and Millero F.J. (2010) Calculating density of water in geochemical lake
656 stratification models. *Limnol. Oceanogr. Methods* **8**, 567–574.

657 Brophy G.P., Scott E.S. and Snellgrove R.A. (1962) Sulfate studies. II. Solid solution between alunite and
658 jarosite. *Amer. Min.* **47**, 112-126.

659 Burger P.V., Papike J.J., Shearer C.K. and Karner J.M. (2009) Jarosite growth zoning as a recorder of fluid
660 evolution. *Geochim Cosmochim Acta* **73**, 3248-3259.

661 Burton E.D., Bush R.T., Johnston S.G., Watling K.M., Hocking R.K., Sullivan L.A., Parker G.K. (2009) Sorption
662 of Arsenic(V) and Arsenic(III) to Schwertmannite. *Environ. Sci. Technol.* **43-24**, 9202–9207.

663 Cornell R.M. and Schwertmann U. (2003) The Iron Oxides: Structure, Properties, Reactions, Occurrences and
664 Uses (2nd Ed.). Wiley-VCH Verlag, Weinheim, 664 p.

665 Davies C.W. (1962) Ion Association. London: Butterworths, pp. 37–53.

666 Diez-Ercilla M., López-Pamo E. and Sánchez-España J. (2009) The photoreduction of Fe(III) in the acidic mine
667 pit lake of San Telmo (Huelva, Spain): Field and laboratory work. *Aquatic Geochemistry* **15**, 391-419.

668 Diez-Ercilla M., Sánchez-España J., Yusta I., Wendt-Potthoff K. and Koschorreck M. (2014) Formation of
669 biogenic sulphides in the water column of an acidic pit lake: Biogeochemical controls and effects on trace
670 metal dynamics. *Biogeochemistry* **121-3**, 519-536.

671 Driscoll C.T., Baker J.P., Bisogni J.J. and Schofield C.L. (1984) Aluminum speciation and equilibria in dilute
672 acidic surface waters of the Adirondack region of New York Sate. In: *Geological aspects of acid deposition*,
673 4: 55-75. Bricker OP (Ed.) Ann Arbor Science, Boston.

674 Dutrizac J.E. and Jambor J.L. (2000) Jarosites and their application in hydrometallurgy. In Sulfate Minerals:
675 Crystallography, Geochemistry, and Environmental Significance (Alpers C.N., Jambor J.L. and Nordstrom
676 D.K., Eds.*). Reviews Miner. Geochem.* **40**, 405-452.

677 Eary L.E. (1999) Geochemical and equilibrium trends in mine pit lakes. *App. Geochemistry* **14**, 963-987.

678 Eary L.E. and Castendyk D.N. (2013) Hardrock metal mine pit lakes: Occurrence and geochemical
679 characteristics. In: Geller, W., Schultze, M., Kleinmann, B., Wolkersdorfern, C. (eds.), *Acidic Pit Lakes: The*
680 *Legacy of Coal and Metal Surface Mines*. Springer-Verlag, Berlin, Heidelberg, pp. 75–106.

681 Falagán C., Sánchez-España J. and Johnson D.B. (2014) New insights into the Biogeochemistry of extremely
682 acidic environments revealed by a combined cultivation-based and culture-independent study of two stratified
683 pit lakes. *FEMS Microbiol Ecol* **87-1**, 231-43.

684 Forray F.L., Smith A.M.L., Navrotsky A., Wright K., Hudson-Edwards K.A., Dubbin W.E. (2014) Synthesis,
685 characterization and thermochemistry of synthetic Pb-As, Pb-Cu and Pb-Zn jarosites. *Geochim Cosmochim*
686 *Acta* **127**, 107-119.

687 Friel J.J. (2003) X-ray and image analysis in electron microscopy. Princeton Gamma-Tech, 2nd Ed., 98 p.

688 Garcidueñas R. and Cervantes C. (1996) Microbial interactions with aluminum. *BioMetals* **9**, 311-316.

689 Garratt-Reed A.J. and Bell D.C. (2003) Energy-Dispersive X-Ray Analysis in the Electron Microscope. BIOS
690 Scientific Publishers Limited, Oxford, UK, 160 p.

691 Härtig C., Brand P. and Bohmhammel K. (1984) Fe-Al isomorphie und strukturwasser in kristallen von Jarosite-
692 Alunit-Typ. *Z. Anorg. Allg. Chem.* **508**, 159-164.

693 Hendershot W.H., Courchesne F. and Jeffries D.S. (1996) Aluminum geochemistry at the catchment scale in
694 watersheds influenced by acidic precipitation. In: Sposito G. (Ed.), *The Environmental Chemistry of*
695 *Aluminum*, 2nd ed., Lewis Publishers-CRC Press LLC, Boca Raton, Florida, pp 419-449.

Jamieson H., Robinson C., Alpers C., Nordstrom D.K., Poustovetov A., Lowers H.A. (2005) The composition of coexisting jarosite-group minerals and water from the Richmond mine, Iron Mountain, California. *The Canadian Mineralogist* **43**, 1225-1242.

Jones A.M., Collins R.N. and Waite T.D. (2011) Mineral species control of aluminum solubility in sulfate-rich acidic waters. *Geochim Cosmochim Acta* **75**, 965-977.

Karathanasis A.D., Evangelou V.P. and Thompson Y.L. (1988) Aluminum and iron equilbria in soil solutions and surface waters of acid mine watersheds. *J. Envirn. Qual*. **17-4**, 534-543.

Keith W.J., Calk L. and Ashley R.P. (1979) Crystals of coexisting alunite and jarosite, Goldfield, Nevada. *Shorter Contrib. Miner. Petr*. **1124-C**, C1-C5, Geological Survey Professional Paper.

Lindsay W.L. and Walthall P.M. (1996) The solubility of aluminum in soils. In: Sposito G. (Ed.), *The Environmental Chemistry of Aluminum,* 2nd ed., Lewis Publishers-CRC Press LLC, Boca Raton, Florida, pp 333-361.

Mosley L.M., Shand P., Self P., and Fitzpatrick R. (2014a) The geochemistry during management of lake acidification caused by the rewetting of sulfuric (pH<4) acid sulfate soils. *Applied Geochemistry* **41**, 49-56.

Mosley L.M., Palmer D., Leyden E., Fitzpatrick R., and Shand P. (2014b) Changes in acidity and metal geochemistry in soils, groundwater, drain and river water in the Lower Murray River after a severe drought. *Science of the Total Environment* **485-486**, 281-291.

Newbury D.E. and Ritchie N.W.M. (2013a) Elemental mapping of microstructures by scanning electron microscopy-energy dispersive X-ray spectrometry (SEM-EDS): extraordinary advances with the silicon drift detector (SDD). *J. Anal. At. Spectrom.* **28**, 973.

Newbury D.E. and Ritchie N.W.M. (2013b) Is Scanning Electron Microscopy/Energy Dispersive X-ray Spectrometry (SEM/EDS) Quantitative?. *Scanning Vol.* **35-3**, 141–168.

Nordstrom D.K. (1982) The effect of sulfate on aluminum concentrations in natural waters: some stability relations in the system Al_2O_3-SO_3-H_2O at 298 K. *Geochim. Cosmochim. Acta* **46**, 681-692.

Nordstrom D.K. and Alpers C.N. (1999) Geochemistry of acid mine waters. In: Plumlee, G.S., and Logsdon, M.J. (eds.), The Environmental Geochemistry of Mineral Deposits, Part A. Processes, Techniques, and Health Issues: Society of Economic Geologists, *Rev. Econ. Geology* **6A**, 133-156.

Nordstrom D.K. and Ball J.W. (1986) The geochemical behavior of aluminum in acidified surface waters. *Science* **232**, 54-56.

Papike J.J., Karner J.M., Spilde M.N. and Shearer C.K. (2006) Terrestrial analogs of martian sulfates: Major and minor element systematics of alunite-jarosite from Goldfield, Nevada. *American Mineralogist* **91**, 1197-1200.

Parkhurst D.L. and Appelo C.A.J. (2013) Description of input and examples for PHREEQC version 3-A computer program for speciation, batch-reactions, one-dimensional transport, and inverse geochemical calculations. In: *Groundwater Book 6, Modeling Techniques*. U.S. Geological Survey, Denver, Colorado, p. 497.

Rancourt D.G. and Ping, J. Y. (1991) Voigt-based methods for arbitrary shape static hyperfine parameter distributions in Mössbauer spectroscopy. *Nucl. Instrum. Meth. B.* **58-1**, 85-97.

Regenspurg S. (2002) Characterisation of Schwertmannite - Geochemical Interactions with Arsenate and Chromate and Significance in Sediments of Lignite Opencast Lakes. PhD Dissertation, University of Bayreuth, 125 p.

Regenspurg S. and Peiffer S. (2005) Arsenate and chromate incorporation in schwertmannite. *Applied Geochemistry* **20**, 1226-1239.

Ripmeester J.A., Ratcliffe C.I., Dutrizac J.E. and Jambor J.L. (1986) Hydronium ion in the alunite-jarosite group. *Can. Mineral.* **24**, 435-447.

Sánchez-España J. (2007) The behavior of iron and aluminum in acid mine drainage: Speciation, Mineralogy, and Environmental Significance. In T.M. Letcher (ed.), *Thermodynamics, Solubility and Environmental Issues*, Elsevier B.V., The Netherlands, pp. 137-149.

Sánchez-España J., López Pamo E., Santofimia E., Aduvire O., Reyes J. and Barettino D. (2005) Acid Mine Drainage in the Iberian Pyrite Belt (Odiel river watershed, Huelva, SW Spain): Geochemistry, Mineralogy and Environmental Implications. *Applied Geochemistry* **20-7**, 1320-1356.

Sánchez-España J., López-Pamo E., Santofimia E., Reyes J. and Martín Rubí J.A. (2006) The removal of dissolved metals by hydroxysulfate precipitates during oxidation and neutralization of acid mine waters, Iberian Pyrite Belt. *Aquat Geochem* **12**, 269-298.

Sánchez-España J., López-Pamo E., Diez M. and Santofimia E. (2009) Physico-chemical gradients and meromictic stratification in Cueva de la Mora and other acidic pit lakes of the Iberian Pyrite Belt. *Mine Water Environ* **28**, 15-29.

Sánchez-España J., Yusta I. and Diez M. (2011) Schwertmannite and hydrobasaluminite: A re-evaluation of their solubility and control on the iron and aluminum concentration in acidic pit lakes. *Applied Geochemistry* **26**, 1752-1774.

Sánchez-España J., Yusta I. and López G. (2012) Schwertmannite to jarosite conversion in the water column of an acidic mine pit lake. *Mineralogical Magazine* **76-7**, 1233-1256.

Sánchez-España J., Diez M. and Santofimia E. (2013) Mine pit lakes of the Iberian Pyrite Belt: Some basic limnological, hydrogeochemical and microbiological considerations. In: Geller, W., Schultze, M., Kleinmann, B., Wolkersdorfern, C. (eds.), *Acidic Pit Lakes: The Legacy of Coal and Metal Surface Mines.* Springer-Verlag, Berlin, Heidelberg, pp. 315–342.

Sánchez-España J., Boehrer B. and Yusta I. (2014) Extreme carbon dioxide concentration in acidic pit lakes provoked by water/rock interaction. *Environ. Sci. Technol*. **48-8**, 4273–4281.

Singh S.S. (1982) The formation and coexistence of gibbsite, boehmite, alumina and alunite at room temperature. *Can J. Scoil Sci.* **62**, 327-332.

765 Stoffregen R.E., Alpers C.N. and Jambor J.L. (2000) Alunite-Jarosite crystallography, thermodynamics, and
766 geochronology. In Sulfate Minerals: Crystallography, Geochemistry, and Environmental Significance (Alpers,
767 C.N., Jambor, J.L., Nordstrom, D.K., Eds.). *Reviews Miner Geochem*, **40**, 453-479.

768 Van Breemen N. (1973) Dissolved aluminum in acid sulfate soils and in acid mine waters. *Soil Sci Soc Amer*
769 *Proc* **37**, 694-697.

770 Wendt-Potthoff K., Koschorreck M., Diez M. and Sánchez-España J. (2012) High microbial activity in a
771 nutrient-rich, acidic mine pit lake. *Limnologica* **42-3**, 175-188.

772 Zhu C. and Burden D.S. (2001) Mineralogical compositions of aquifer matrix as necessary initial conditions in
773 reactive contaminant transport models. *J Contam Hydrology* **51**, 145-161.

774

TABLE CAPTIONS

Table 1. Chemical composition of San Telmo acidic mine pit lake at several depths, as measured in July 2010.

Table 2. Chemical composition of schwertmannite particles formed at different depths in various acid pit lakes of the IPB (ST, San Telmo, HER, Herrerías, CM, Cueva de la Mora), as obtained by Energy Dispersion Spectroscopy (EDS) coupled to a Titan3 (FEI) transmission electron microscope (TEM).

Table 3. Chemical composition of selected jarosite and alunite crystals formed at different depths in the San Telmo acid pit lake (ST), as obtained by Energy Dispersion Spectroscopy (EDS) coupled to a Titan (FEI) transmission electron microscope (TEM). Analyses for crystals from Cueva de la Mora (CM) are also included. Data in plain text denote whole crystal analyses, while data in italics represent partial analyses of either cores or rims of chemically zoned crystals (see Figures 7-8).

FIGURE CAPTIONS

Figure 1. Approximate geographical situation **(a)**, field and satellite images **(b-c)**, Oxidation-reduction potential (ORP) **(d)** and pH **(e)** of the San Telmo pit lake, Huelva (SW Spain) (modified from Sánchez-España et al., 2012). Satellite image taken from Google Earth.

Figure 2. Vertical profiles of element concentration in the San Telmo acidic pit lake (as measured in July 2010 –*open symbols*; taken from Sánchez-España et al., 2012– and April 2011 –*black symbols*–): **(a)** Fe and Al; **(b)** K and Na, **(c)** As and Cr, and **(d)** Mo and Pb. All element concentrations given in molar proportion.

Figure 3. Scanning electron microscope (SEM; a-b) and transmission electron microscope (TEM; c-d) photomicrographs of jarosite and/or alunite crystals formed at different depths in the water column of the San Telmo (a-b) and Cueva de la Mora (c-d) acid pit lakes. The concentrations of major elements in the analysed crystals are shown in a-b: **(a)** Al-rich jarosite crystal growing in schwertmannite groundmass formed in deep anoxic waters at 100 m depth (note the holes produced by the electronic beam during the EDS analyses); **(b)** Isolated crystal of Fe-rich alunite formed at 100 m depth. **(c-d)** TEM images of

concentrically zoned jarosite crystals. Scale bar is 100 nm in (c) and 80 nm in (d). *Abbreviations: Sch, schwertmannite; Jar, jarosite; Alu, alunite.*

Figure 4. Chemical mapping of an aggregate of schwertmannite nanoparticles formed at 40 m depth in the San Telmo acid pit lake, as obtained by Energy Dispersion Spectroscopy (EDS) with a Transmission Electron Microscope under Scanning mode (STEM): **(a)** High Angle Annular Dark Field (HAADF) image without any element filter; **(b)** Mapping of S element distribution; **(c)** Mapping of Fe element distribution; **(d)** Mapping of Al element distribution.

Figure 5. (a) Plot of the Fe/[Fe+Al] ratio *vs*. pH for the analysed schwertmannite particles from the San Telmo acid pit lake; the error bars are shown for every data point; the inset shows enlargement of the Y axis to better display the analyses within the range Fe/[Fe+Al]=0.75-1.00. **(b)** Chemical model of aluminium ionic species distribution for the pH range 0-8 (computed with PHREEQC for a_{SO4}=0.1 M and a_{Al}=0.03 M; taken from Sanchez-España, 2007, with permission from Springer). The shaded area represents the pH window considered in this study. The approximate pH intervals for the observed Fe(III)-Al coprecipitation and Al adsorption are also indicated.

Figure 6. Aluminum and iron distributions within a schwertmannite nanoparticle formed at 100 m depth in the San Telmo acid pit lake, as obtained by STEM-EDS: **(a)** High Angle Annular Dark Field (HAADF) image without any element filter; **(b)** Mapping of Fe and Al element distribution along with obtained compositions for selected core and edge (needles) areas (in *at.%*; given as HER65 Particle 6 in Table 2); **(c)** Transversal composition (*line scanning*) across the schwertmannite particle, along with the obtained Al and Fe relative concentration **(d)**. An outer shell of adsorbed Al (likely composed of $AlSO_4^-$ and/or $AlSO_4^+$ complexes) is clearly visible around the Fe-containing schwertmannite needles.

Figure 7. (a) Chemical mapping showing the distribution of aluminium and iron in alunite (Alu) and jarosite (Jar) crystals formed at 100 m depth in the San Telmo acid pit lake, as obtained by STEM-EDS; note the different composition of the crystal on the left (in red, only composed of Al) with respect to the crystal on the right (showing an evident zonation with an Al-rich core –in red- surrounded by an Fe-rich rim –in blue-; **(b)** *Line scanning* across the zoned crystal on the right (indicated by a transversal yellow line in *(a)*) showing the relative concentration of Al and Fe throughout the crystal. Based on the chemical composition of selected areas within this crystal (given as *ST100/8_core* and *ST100/8_rim*

838 in Table 3) the core is formed by Fe-containing alunite while the rim corresponds to Al-
839 containing jarosite.

840 **Figure 8.** Chemical mapping of a zoned jarosite crystal from the San Telmo acid pit lake, as
841 obtained by STEM-EDS: **(a)** Al; **(b)** Fe; **(c)** Al and Fe; **(d)** Al and Fe superimposed on the
842 HAADF image, with indication of the area selected as "*core*" in Table 3
843 (*ST100N14/6_core*); **(e)** same as *(d)*, with indication of the area selected as "*rim*" in Table
844 3 (*ST100N14/6_rim*); **(f)** same as *(d)*, with indication of the *line scan* (transversal yellow
845 line) across the zoned crystal; **(g)** transversal scanning shown in *(f)* showing the relative
846 concentration of Al and Fe throughout the crystal.

847 **Figure 9.** Chemical mapping of an homogenous alunite crystal from the San Telmo acid pit
848 lake, as obtained by STEM-EDS: **(a)** Al; **(b)** S; **(c)** Fe; **(d)** Al and Fe with indication of a
849 *line scan* (transversal yellow line) conducted across the crystal; **(e)** same as *(d)*, with
850 indication of the area selected for the whole crystal analyses labelled as *ST100/8_wcII in*
851 *Table 3*; **(f)** K; **(g)** Results of the line scan shown in *(d)* with the relative concentration of
852 Al and Fe throughout the crystal. The iron-rich material outside the alunite crystal is made
853 of nanometric particles of schwertmannite adhered to the crystal edges.

854 **Figure 10.** High resolution images obtained by transmission electron microscopy (HRTEM)
855 for outer areas in selected crystals of jarosite **(a)** and alunite **(b)**. The chemical composition
856 of these two crystals is also given in Table 3 (ST100-22/1 and ST100N14/9, respectively).
857 The main diffraction rings and spots are given in the insets, and the corresponding d-
858 spacings are also indicated.

859 **Figure 11.** Composition of jarosites and alunites formed in the water column of the San
860 Telmo, Herrerías and Cueva de la Mora acid pit lakes: **(a)** Binary plot of Al *vs*. Fe (given as
861 *wt.%*); **(b)** Classification in a plot of $[Fe/(Fe+Al)]_m$ *vs*. $[H_3O^+/(H_3O^+ + K^+)]_m$. The
862 compositions have been obtained by SEM-EDS and/or STEM-EDS. The ideal composition
863 of the pure end-members (H_3O^+-jarosite, *red star*; alunite, *blue star*) is also indicated.

864 **Figure 12.** Vertical evolution of saturation indices for selected mineral phases across the
865 water column of the San Telmo acid mine pit lake (modified from Sánchez-España et al.,
866 2012). Calculations computed with PHREEQC using field data and element concentrations
867 obtained in two different seasons (June 2006 –**a**– and April 2011 –**b**–). Abbreviations:
868 Schw, schwertmannite; Jar-H_3O, Hydronian jarosite; Jar-K, Potassium jarosite; Alu,
869 alunite; Goet, goethite; Gib, gibbsite.

870 **Figure 13. (a)** Plot of the saturation index for selected mineral phases *vs*. pH in the San Telmo
871 acid pit lake (modified from Sánchez-España et al., 2012). The samples and chemical data
872 used to produce this plot are the same as those used in Fig. 12 plus some additional samples
873 taken in September 2008 from the same lake (Fig. 1) **(b)** pH-pe plot for the Al-Fe-S-K-O-H
874 system with proposed stability fields for common mineral sinks of dissolved Al. The
875 Fe(III) species have been also considered to include the incorporation of Al at pH<3.3. The
876 symbols (white circles, San Telmo; grey triangles, Cueva de la Mora) indicate the pH- pe
877 conditions observed in waters of different depths in the studied pit lakes. *Abbreviations*:
878 Schw, schwertmannite; Jar-H_3O, Hydronian jarosite; Jar-K, Potassium jarosite; Alu,
879 alunite; Hybs, hydrobasaluminite; Fsbn, felsobanyaite; Gibb, gibbsite.

880

Table 1. Chemical composition of the San Telmo acid mine pit lake at several depths, as measured in July 2010.

	Major cations									Major anions					
Depth	**Na**	**K**	**Mg**	**Ca**	**Fe**	**Al**	**Mn**	**Cu**	**Zn**	**SO_4^{2-}**	**Cl^-**	**NO_3^-**	**SiO_2**	**DOC**	**DIC**
m	*mg/L*	*mg/L*	*mg/L*	*mg/L*	*mg/L*	*mg/L*	*mg/L*	*mg/L*	*mg/L*	*g/l*	*mg/L*	µg/L	*mg/L*	*mg/L*	*mg/L*
0	17	2.3	472	231	114	145	38	18	76	3.6	16	18	58	1.1	35
10	20	1.5	551	296	183	183	49	24	93	4.5	15	16	66	1.2	48
25	20	1.6	579	302	186	182	50	25	96	4.5	14	17	68	1.0	52
30	23	1.3	625	375	164	180	59	27	107	5.1	14	10	63	0.9	114
60	24	1.2	648	425	156	160	65	28	114	4.8	13	6	61	0.8	110
90	25	1.1	666	425	146	145	65	28	114	4.9	14	6	60	0.6	105

	Trace elements															
Depth	**As**	**Ag**	**Se**	**Be**	**Ba**	**Cd**	**Co**	**Cr**	**Mo**	**Ni**	**Pb**	**Sb**	**Th**	**Tl**	**U**	**V**
m	*µg/L*	*µg/L*	*µg/L*	*µg/L*	*µg/L*	*µg/L*	*µg/L*	*µg/L*	*µg/L*	*µg/L*	*µg/L*	*µg/L*	*µg/L*	*µg/L*	*µg/L*	*µg/L*
0	14	b.d.	51	27	16	179	875	14	4	417	56	b.d.	5	3	19	b.d.
10	70	b.d.	72	35	15	243	1.148	21	5	524	71	b.d.	8	3	25	b.d.
25	67	b.d.	69	31	26	245	1.148	21	3	524	70	b.d.	8	3	25	b.d.
30	27	b.d.	75	34	7	267	1.355	18	2	579	44	b.d.	8	3	27	b.d.
60	20	b.d.	78	35	12	287	1.511	17	2	626	19	b.d.	8	3	29	b.d.
90	21	b.d.	78	35	14	288	1.496	17	1	621	19	b.d.	8	3	30	b.d.

b.d., *below detection limit (0.2 µg/L)*

Table 2. Chemical composition of schwertmannite particles formed at different depths in various acid pit lakes of the IPB (ST, San Telmo, HER, Herrerías, CM, Cueva de la Mora), as obtained by Energy Dispersion Spectroscopy (EDS) coupled to a scanning transmission electron microscope (STEM).

Sample		**O** *at.%*	**Fe** *at.%*	**S** *at.%*	**Al** *at.%*	**Si** *at.%*	**Total** *at.%*	$\frac{Fe}{[Fe+Al]}$	**Fe/S**	**pH**
ST100ox		66.68	24.19	7.05	0.98	0.4	99.30	0.96	3.43	2.6
ST100ox		65.33	28.08	5.89	0.11	0.11	99.52	1.00	4.77	2.6
ST100ox		66.48	26.92	5.77	0.22	0.13	99.52	0.99	4.67	2.6
ST100ox		66.63	27.11	6.02	0.00	0.00	99.76	1.00	4.50	2.6
CM18		64.06	26.74	6.61	0.70	0.99	99.10	0.97	4.05	2.6
ST35		66.35	25.28	6.59	1.20	0.95	100.37	0.95	3.84	2.6
ST99		65.55	26.11	6.12	1.21	1.27	100.25	0.96	4.27	2.8
ST3.5		64.20	26.35	8.22	1.02	0.00	99.79	0.96	3.21	3.5
HER50	Particle 1	64.90	25.16	5.82	3.16	0.14	99.18	0.89	4.32	4.0
HER50	Particle 2	67.73	23.94	5.00	2.56	0.08	99.31	0.90	4.79	4.0
HER50	Particle 3	66.34	24.76	5.23	2.72	0.08	99.13	0.90	4.73	4.0
HER50	Particle 4	63.51	26.35	5.93	3.37	0.06	99.22	0.89	4.44	4.0
HER50	Particle 5	66.07	24.84	5.49	2.78	0.04	99.22	0.90	4.52	4.0
Ideal Schwertmannite		**66.70**	**29.60**	**3.70**	**0.00**	**0.00**	**100.00**		**8.00**	
HER65	Particle 6 (core)	58.25	27.61	4.46	8.19	0.24	98.75	0.77	6.19	4.3
HER65	Particle 7 (core)	54.19	31.10	4.82	8.44	0.51	99.06	0.79	6.45	4.3
HER65	Particle 6 (needles)	64.25	11.67	4.51	17.12	1.24	98.79	0.41	2.59	4.3
HER65	Particle 7 (needles)	62.50	14.41	5.08	15.84	0.14	97.97	0.48	2.84	4.3

Table 3. Chemical composition of selected jarosite and alunite crystals formed at different depths in the San Telmo acid pit lake, as obtained by Energy Dispersion Spectroscopy (EDS) coupled to a scanning transmission electron microscope (STEM). Analyses for crystals from Cueva de la Mora (CM) are also included. Data in plain text denote whole crystal analyses, while data in italics represent partial analyses of either cores or rims of chemically zoned crystals (see Figures 7-8).

Sample	**O**	**S**	**Fe**	**Al**	**K**	**Na**	**Si**	**Total**	**Fe**	**H_3O^+**
	at.%	*at.%*	*at.%*	*at.%*	*at.%*	*at.%*	*at.%*	*at.%*	**[Fe+Al]**	**[H_3O^++K]**
CM36/1	68.28	10.96	16.80	0.38	1.26	1.36	0.24	99.28	0.98	0.75
CM36/2	71.97	10.06	15.14	0.55	0.69	1.06	0.26	99.73	0.96	0.86
ST100-22/1	66.22	12.46	15.45	0.51	4.65	0.34	0.85	100.48	0.97	0.09
ST100-22/2	64.65	11.08	16.99	1.00	2.71	0.16	1.75	98.33	0.94	0.47
ST100-22/3	66.90	11.08	17.39	0.73	2.85	0.15	1.05	100.16	0.96	0.44
ST100-22/4	66.25	9.38	16.25	1.88	2.76	0.21	2.91	99.64	0.90	0.46
ST100-22/5	68.21	11.47	16.35	0.75	2.79	0.28	0.58	100.43	0.96	0.45
ST100-22/6	67.24	11.88	19.19	0.30	0.62	0.45	0.07	99.75	0.98	0.88
ST100/1	70.70	10.50	15.38	0.14	3.17	0.11	0.00	100.00	0.99	0.38
ST100/1.2	68.73	10.24	15.37	0.53	2.87	0.66	1.30	99.70	0.97	0.44
ST100/2	65.34	13.16	15.26	0.32	5.11	0.36	0.44	99.99	0.98	0.00
ST100N14/6_rim	*65.38*	*11.47*	*19.34*	*0.55*	*2.68*	*0.20*	*0.25*	*99.87*	*0.97*	0.47
ST100N14/6_core	*63.84*	*12.52*	*14.19*	*5.56*	*3.24*	*0.31*	*0.21*	*99.87*	*0.72*	0.36
ST100/6_rim	*61.15*	*10.21*	*11.47*	*9.82*	*5.06*	*0.00*	*1.65*	*99.36*	*0.54*	0.01
ST100/8_rim	*61.12*	*11.30*	*16.90*	*2.86*	*4.79*	*1.24*	*1.52*	*99.73*	*0.86*	0.06
ST100N14/7	67.44	9.38	4.66	13.11	3.21	0.76	1.41	99.97	0.26	0.20
ST100N14/9	59.74	10.18	2.68	19.19	6.98	0.58	0.51	99.86	0.12	0.13
ST100/6_core	*57.98*	*10.64*	*4.17*	*18.08*	*7.91*	*0.22*	*0.78*	*99.78*	*0.19*	0.01
ST100/8_core	*61.75*	*11.27*	*7.25*	*12.43*	*6.57*	*0.24*	*0.35*	*99.86*	*0.37*	0.18
ST100/8_core2	*61.55*	*10.92*	*5.56*	*14.15*	*6.89*	*0.47*	*0.46*	*100.00*	*0.28*	0.14
ST100/8_wc	62.63	10.24	7.24	12.47	6.55	0.25	0.36	99.74	0.37	0.18
ST100/8_wcII	63.25	10.35	1.37	17.80	6.19	0.11	0.73	99.80	0.07	0.23
Jarosite (ideal)	70.00	10.00	15.00	0.00	5.00	-	-	100.00	1.00	
H-Jarosite (ideal)	75.00	10.00	15.00	0.00	0.00	-	-	100.00	1.00	
Alunite (ideal)	70.00	10.00	0.00	15.00	5.00	-	-	100.00	0.00	

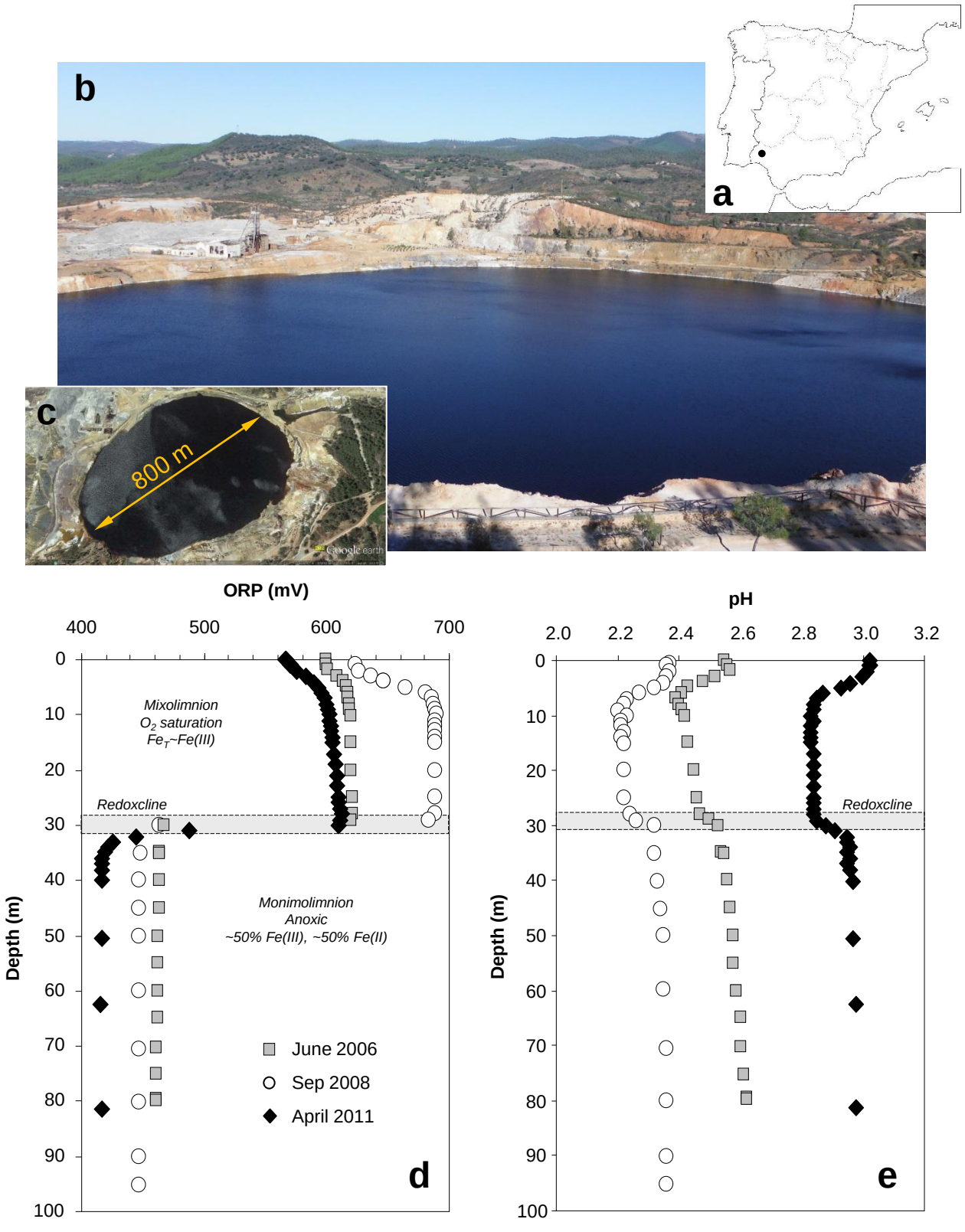
a
b
c
800 m
Google earth
ORP (mV)
400
500
600
700
0
10
20
30
40
50
60
70
80
90
100
Depth (m)
Mixolimnion
O_2 saturation
Fe_T~Fe(III)
Redoxcline
Monimolimnion
Anoxic
~50% Fe(III), ~50% Fe(II)
June 2006
Sep 2008
April 2011
d
pH
2.0
2.2
2.4
2.6
2.8
3.0
3.2
Redoxcline
e

Figure 1

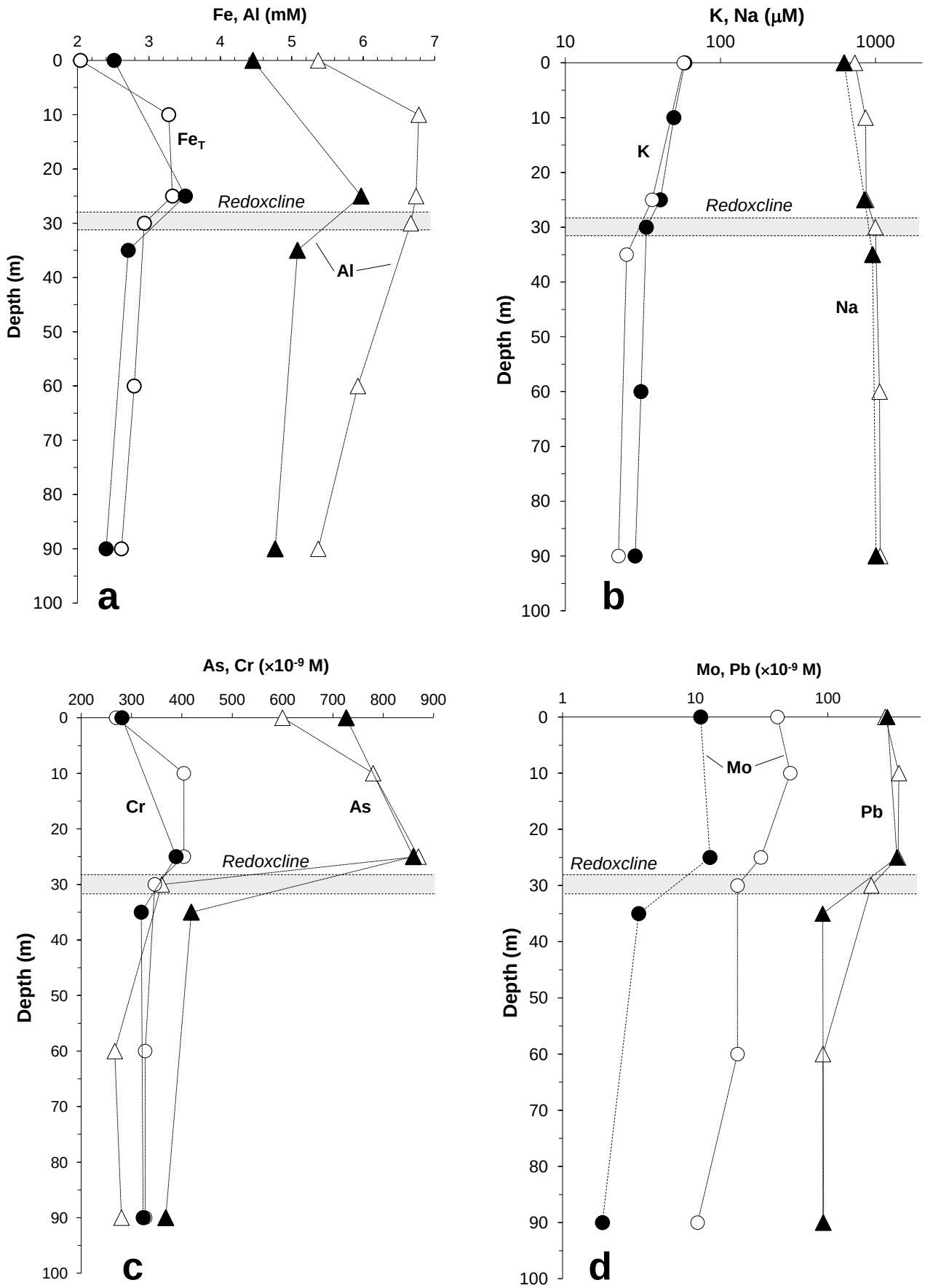
Fe, Al (mM)
Depth (m)
Fe$_T$
Redoxcline
Al
a
K, Na (μM)
K
Redoxcline
Na
b
As, Cr (×10^{-9} M)
Cr
As
Redoxcline
c
Mo, Pb (×10^{-9} M)
Mo
Pb
Redoxcline
d

Figure 2

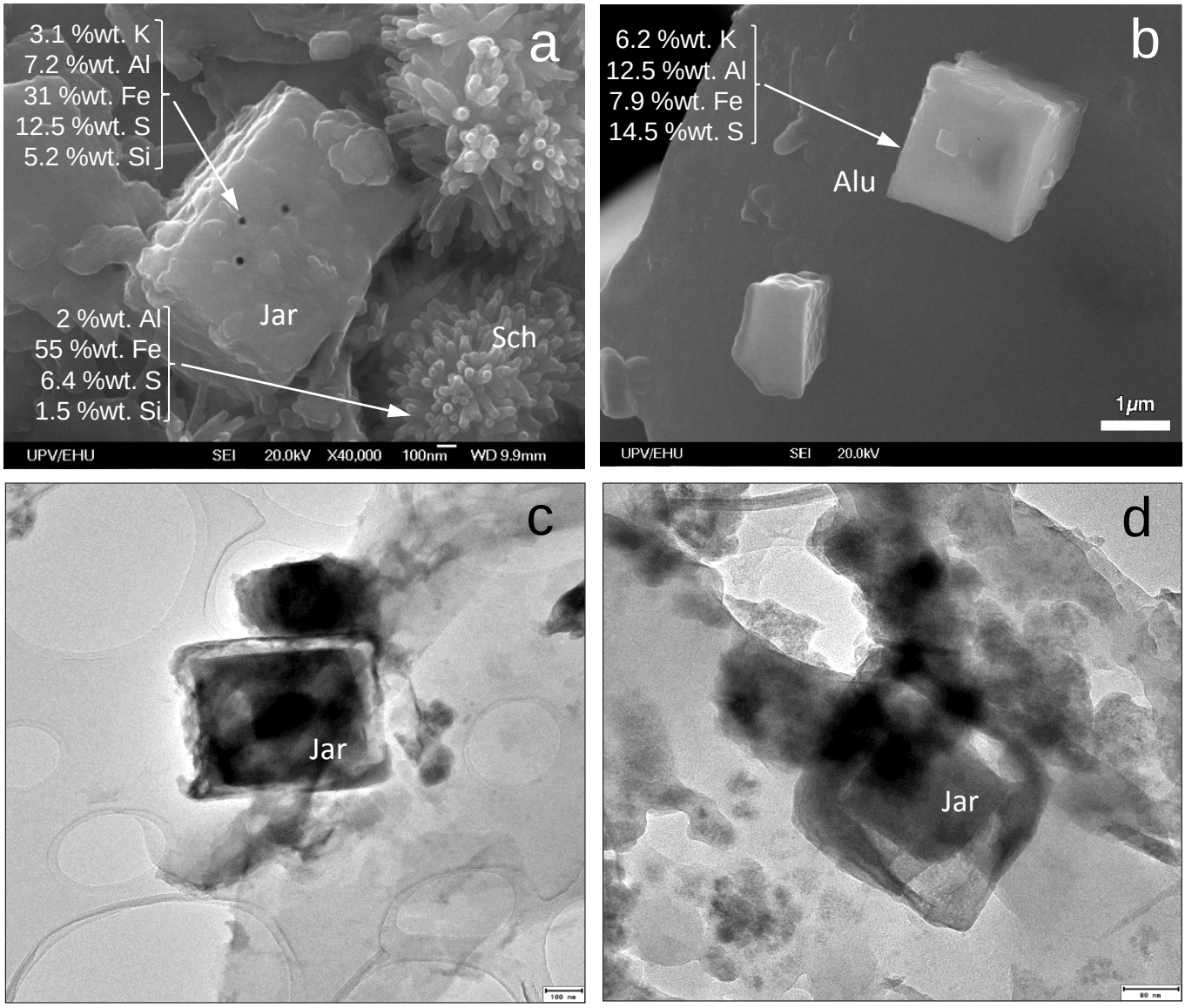
a
3.1 %wt. K
7.2 %wt. Al
31 %wt. Fe
12.5 %wt. S
5.2 %wt. Si
2 %wt. Al
55 %wt. Fe
6.4 %wt. S
1.5 %wt. Si
Jar
Sch
UPV/EHU SEI 20.0kV X40,000 100nm WD 9.9mm
b
6.2 %wt. K
12.5 %wt. Al
7.9 %wt. Fe
14.5 %wt. S
Alu
1μm
UPV/EHU SEI 20.0kV
c
Jar
d
Jar

Figure 3

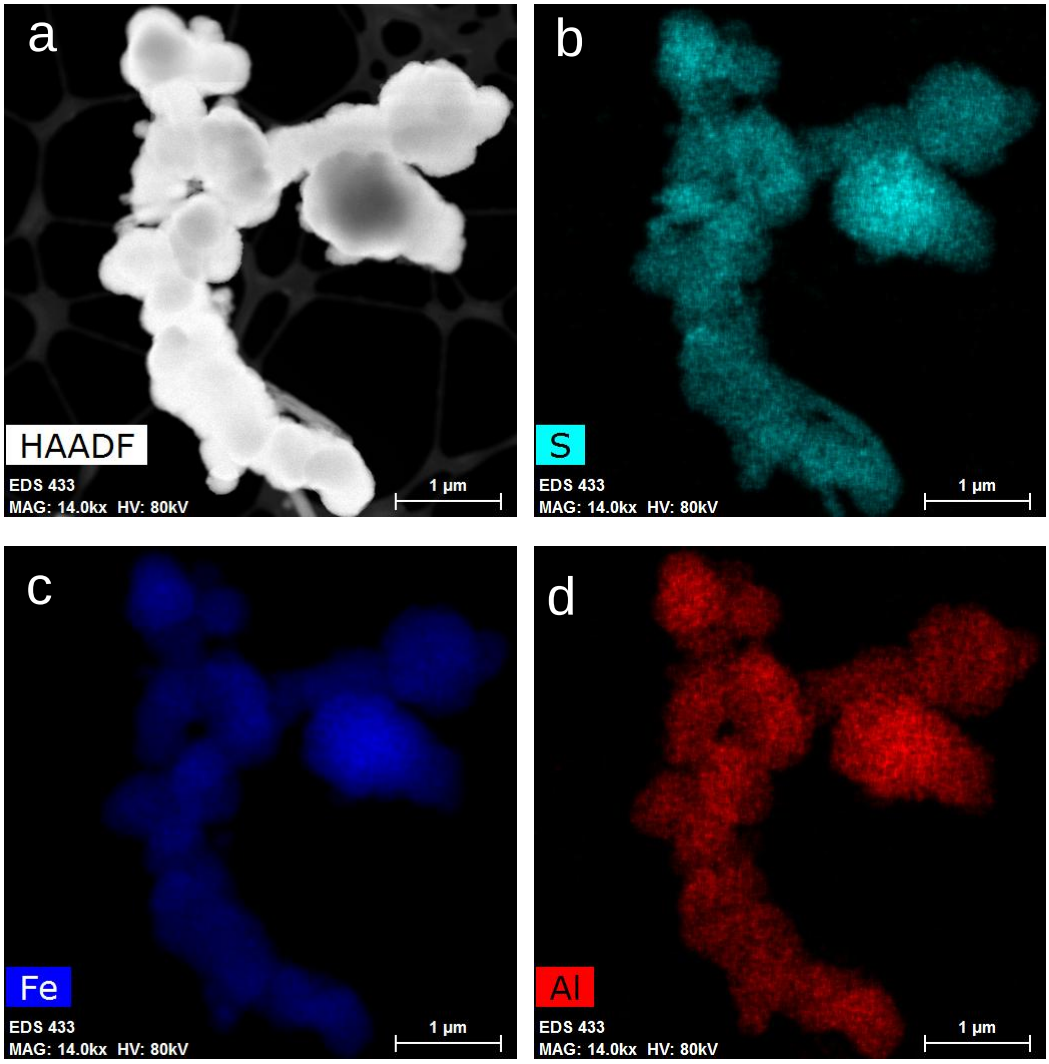
a
HAADF
EDS 433
MAG: 14.0kx HV: 80kV
1 µm
b
S
EDS 433
MAG: 14.0kx HV: 80kV
1 µm
c
Fe
EDS 433
MAG: 14.0kx HV: 80kV
1 µm
d
Al
EDS 433
MAG: 14.0kx HV: 80kV
1 µm

Figure 4

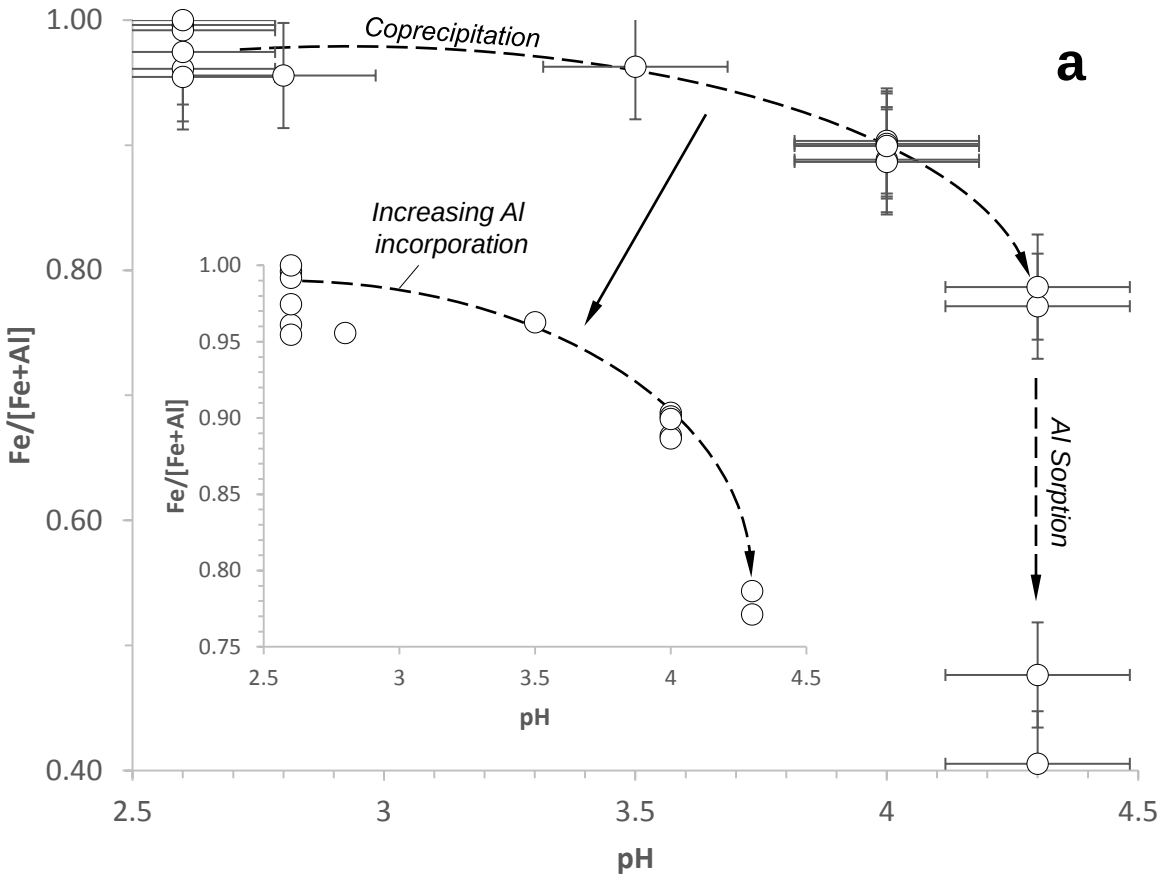
a
Coprecipitation
Increasing Al incorporation
Al Sorption
Fe/[Fe+Al]
pH
1.00
0.80
0.60
0.40
2.5
3
3.5
4
4.5
0.95
0.90
0.85
0.75

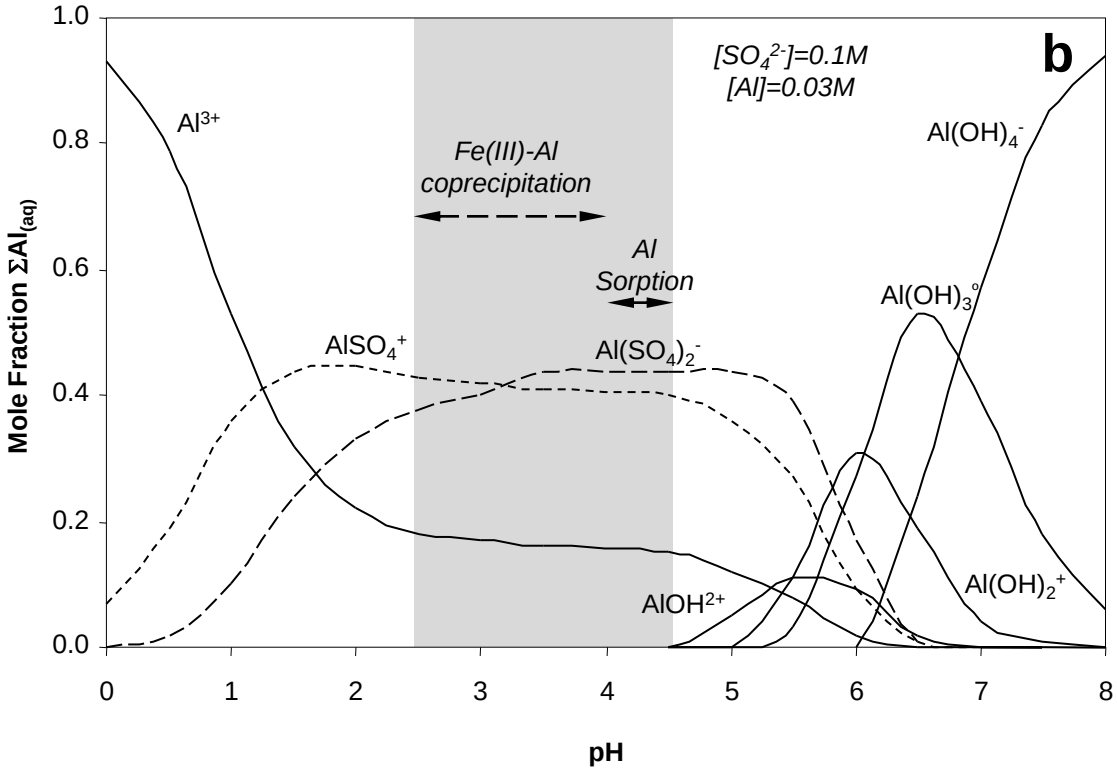
b
[SO4 2-]=0.1M
[Al]=0.03M
Fe(III)-Al coprecipitation
Al Sorption
Al3+
AlSO4+
Al(SO4)2-
AlOH2+
Al(OH)4-
Al(OH)3°
Al(OH)2+
Mole Fraction ΣAl(aq)
pH
1.0
0.8
0.6
0.4
0.2
0.0
0
1
2
3
4
5
6
7
8

Figure 5

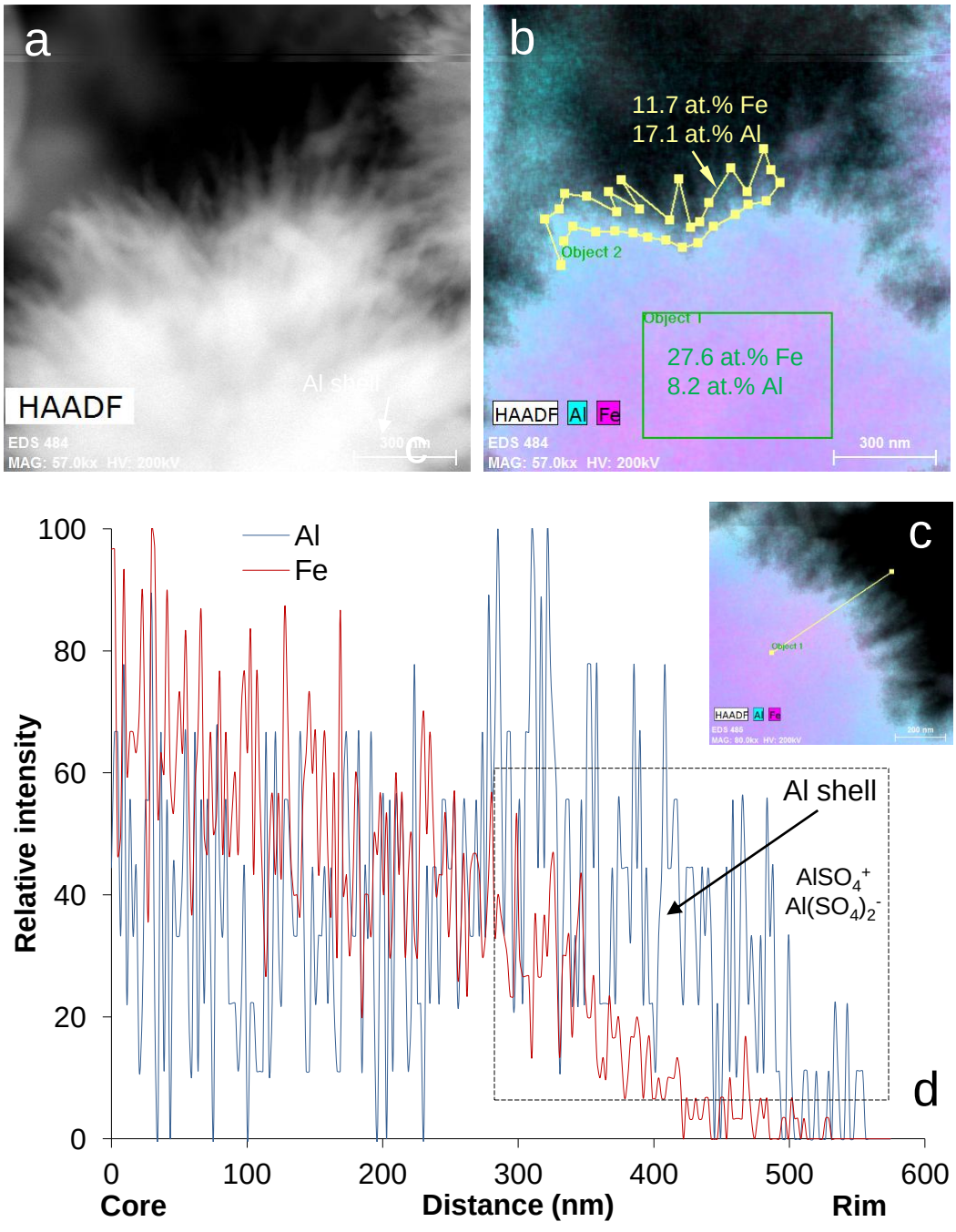
a
HAADF
Al shell
EDS 484
MAG: 57.0kx HV: 200kV
300 nm
b
11.7 at.% Fe
17.1 at.% Al
Object 2
Object 1
27.6 at.% Fe
8.2 at.% Al
HAADF Al Fe
EDS 484
MAG: 57.0kx HV: 200kV
300 nm
c
Object 1
HAADF Al Fe
d
Al
Fe
Relative intensity
Al shell
$AlSO_4^+$
$Al(SO_4)_2^-$
0
20
40
60
80
100
0
100
200
300
400
500
600
Core
Distance (nm)
Rim

Figure 6

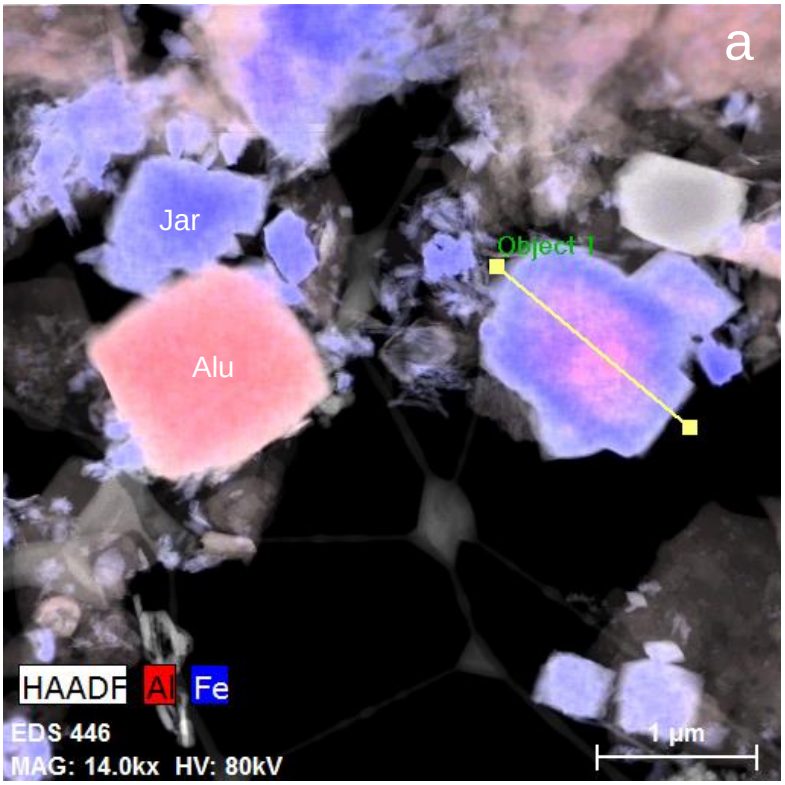
a
Jar
Alu
Object 1
HAADF
Al
Fe
EDS 446
MAG: 14.0kx HV: 80kV
1 µm

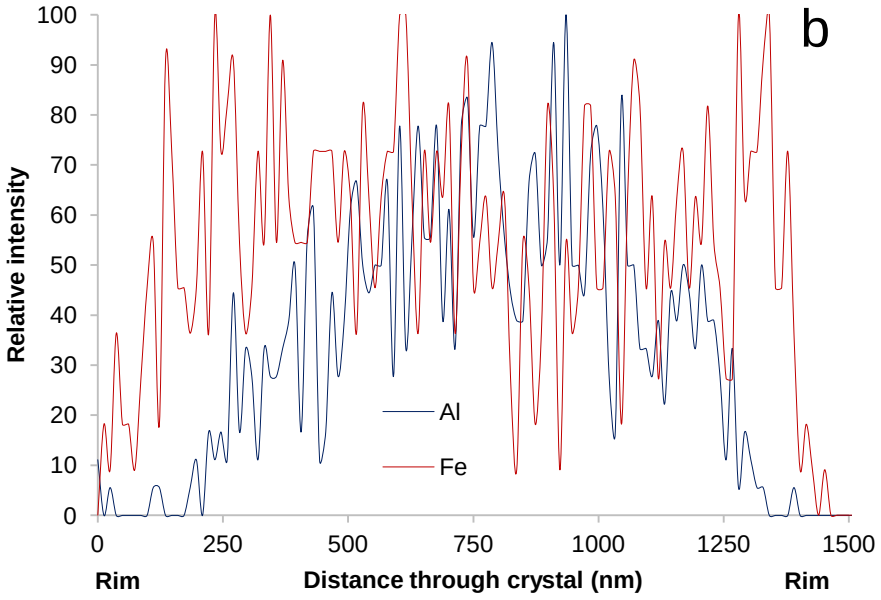
b
Relative intensity
100
90
80
70
60
50
40
30
20
10
0
Al
Fe
0
250
500
750
1000
1250
1500
Rim
Distance through crystal (nm)
Rim

Figure 7

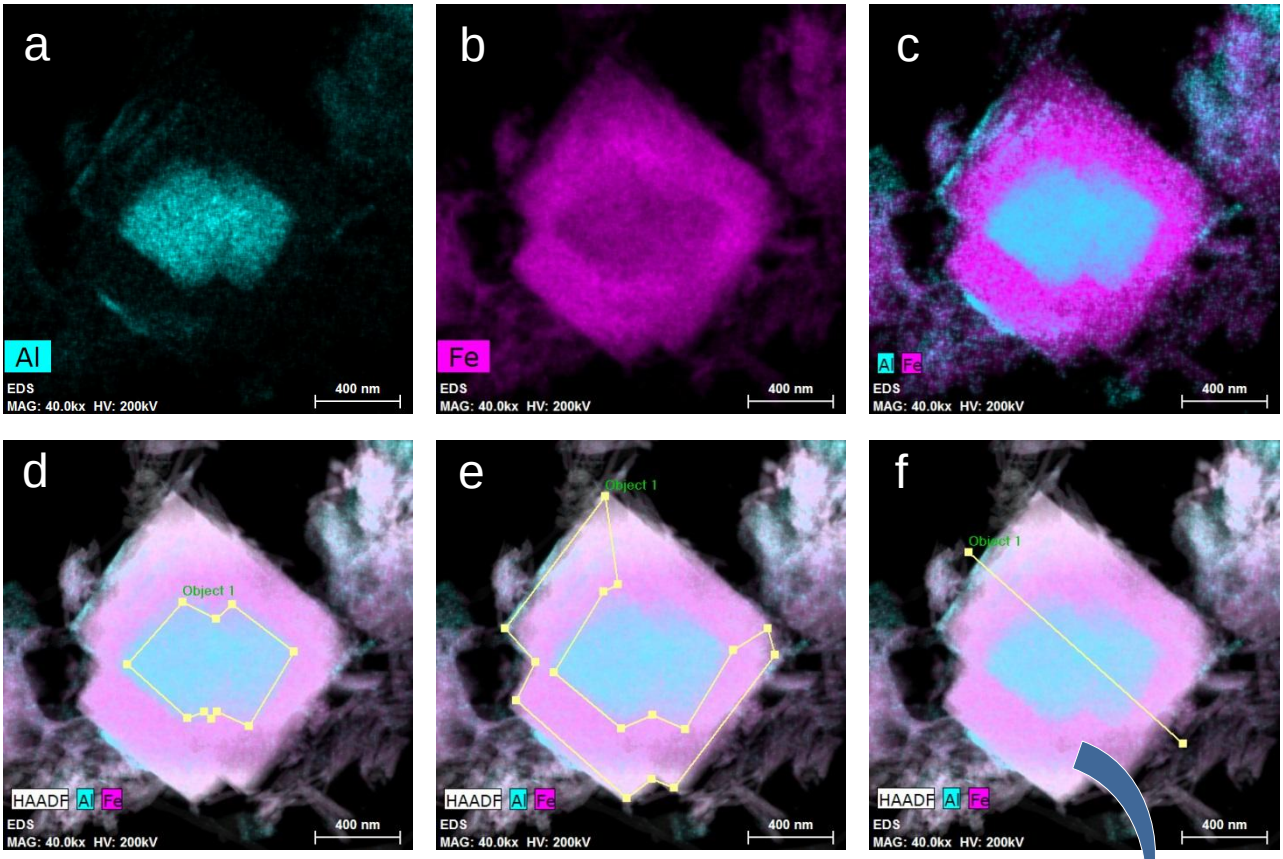
a
Al
EDS
MAG: 40.0kx HV: 200kV
400 nm
b
Fe
EDS
MAG: 40.0kx HV: 200kV
400 nm
c
Al Fe
EDS
MAG: 40.0kx HV: 200kV
400 nm
d
Object 1
HAADF Al Fe
EDS
MAG: 40.0kx HV: 200kV
400 nm
e
Object 1
HAADF Al Fe
EDS
MAG: 40.0kx HV: 200kV
400 nm
f
Object 1
HAADF Al Fe
EDS
MAG: 40.0kx HV: 200kV
400 nm

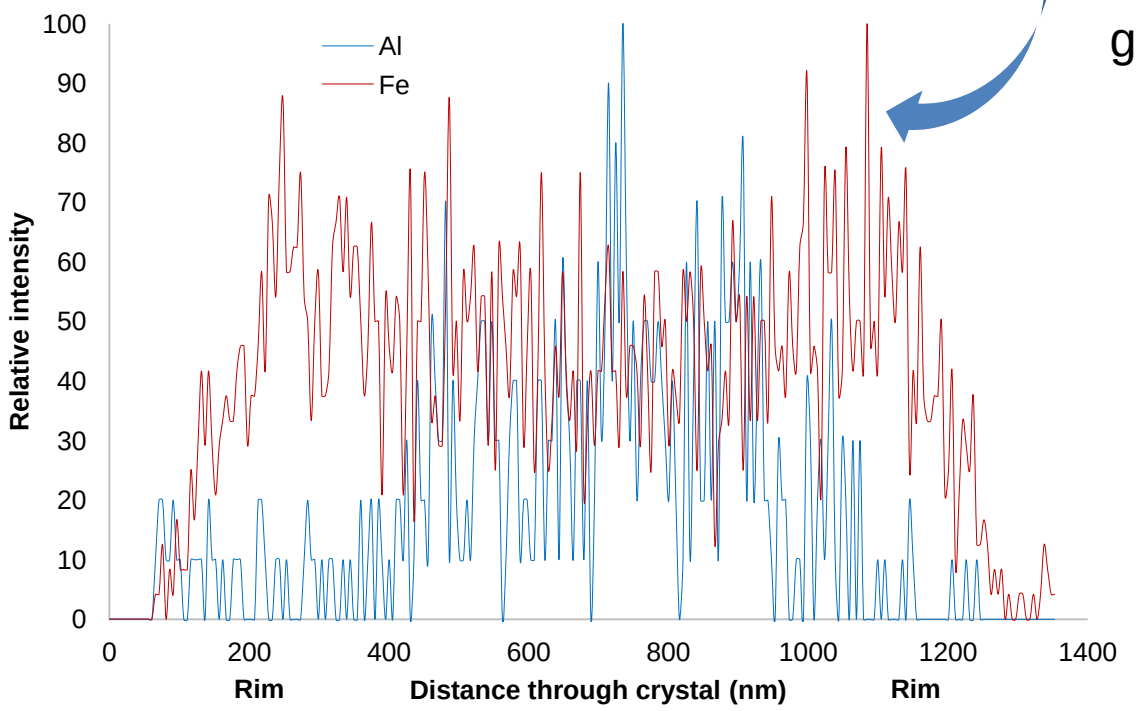
g
Al
Fe
Relative intensity
100
90
80
70
60
50
40
30
20
10
0
0
200
400
600
800
1000
1200
1400
Rim
Distance through crystal (nm)
Rim

Figure 8

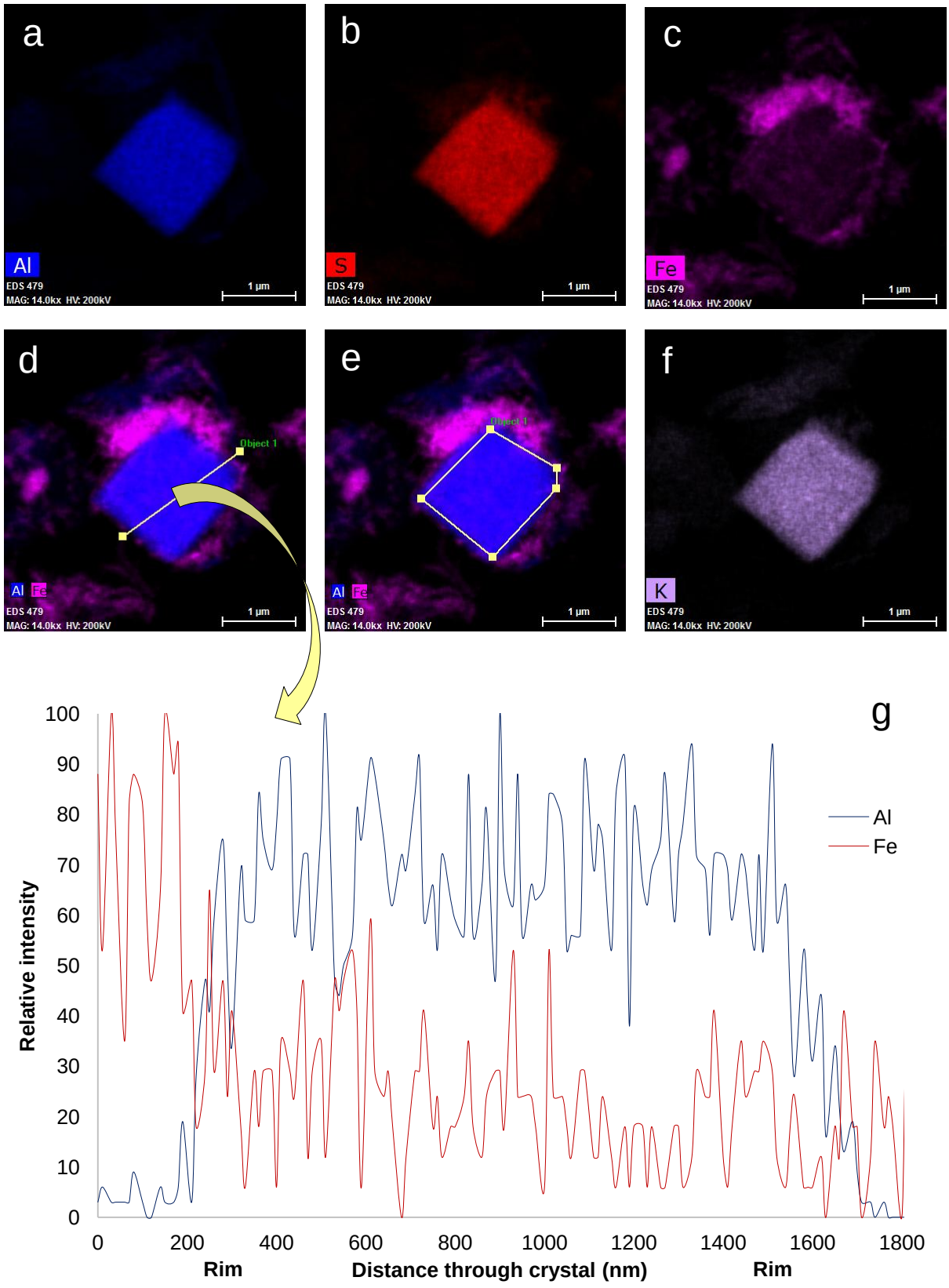
a
Al
EDS 479
MAG: 14.0kx HV: 200kV
1 µm
b
S
EDS 479
MAG: 14.0kx HV: 200kV
1 µm
c
Fe
EDS 479
MAG: 14.0kx HV: 200kV
1 µm
d
Object 1
Al Fe
EDS 479
MAG: 14.0kx HV: 200kV
1 µm
e
Object 1
Al Fe
EDS 479
MAG: 14.0kx HV: 200kV
1 µm
f
K
EDS 479
MAG: 14.0kx HV: 200kV
1 µm
g
Relative intensity
100
90
80
70
60
50
40
30
20
10
0
0
200
400
600
800
1000
1200
1400
1600
1800
Rim
Distance through crystal (nm)
Rim
Al
Fe

Figure 9

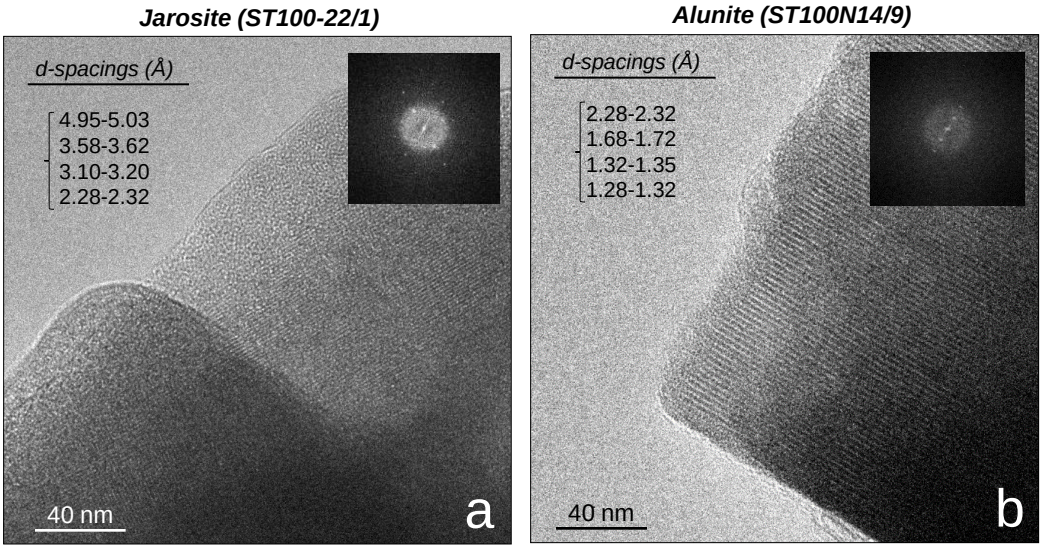
Jarosite (ST100-22/1)
d-spacings (Å)
4.95-5.03
3.58-3.62
3.10-3.20
2.28-2.32
40 nm
a
Alunite (ST100N14/9)
d-spacings (Å)
2.28-2.32
1.68-1.72
1.32-1.35
1.28-1.32
40 nm
b

Figure 10

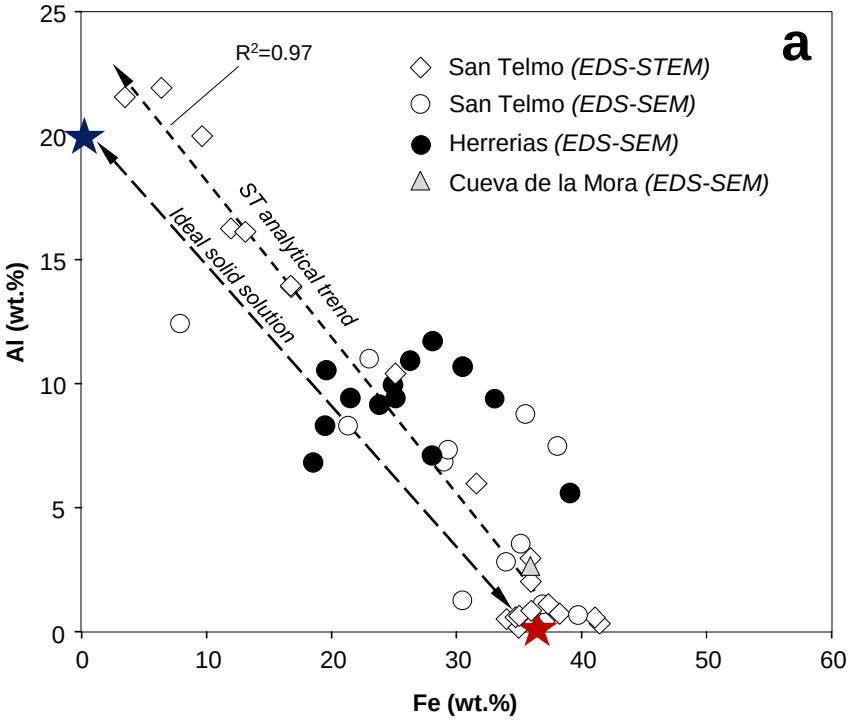
a
R²=0.97
San Telmo (EDS-STEM)
San Telmo (EDS-SEM)
Herrerias (EDS-SEM)
Cueva de la Mora (EDS-SEM)
ST analytical trend
Ideal solid solution
Al (wt.%)
Fe (wt.%)
0
5
10
15
20
25
0
10
20
30
40
50
60

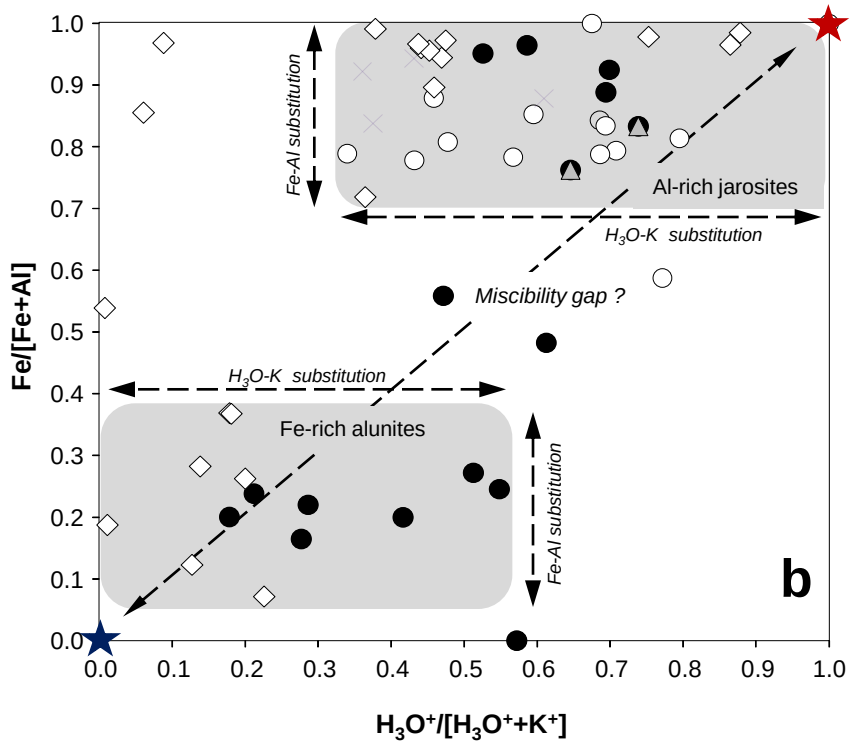
b
Fe-Al substitution
Al-rich jarosites
H3O-K substitution
Miscibility gap ?
H3O-K substitution
Fe-rich alunites
Fe-Al substitution
Fe/[Fe+Al]
H3O+/[H3O++K+]
0.0
0.1
0.2
0.3
0.4
0.5
0.6
0.7
0.8
0.9
1.0

Figure 11

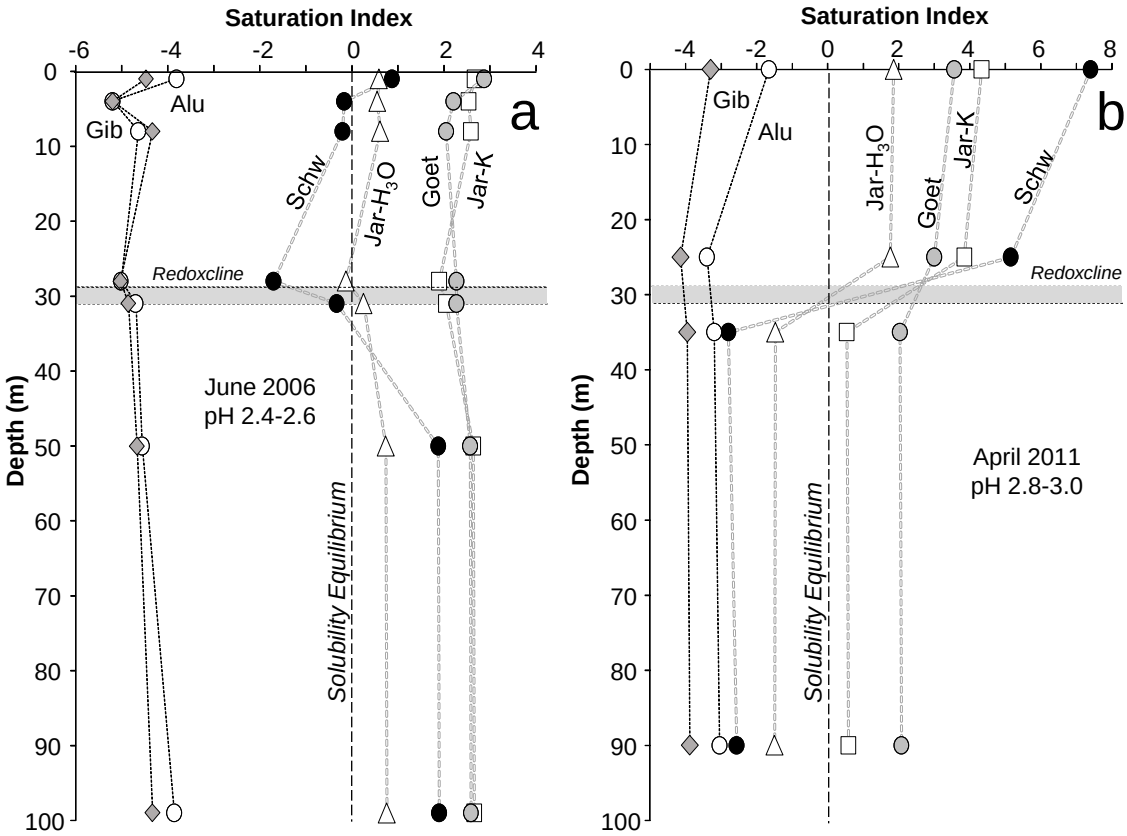
Saturation Index
-6
-4
-2
0
2
4
Depth (m)
0
10
20
30
40
50
60
70
80
90
100
Gib
Alu
Schw
Jar-H3O
Goet
Jar-K
Redoxcline
Solubility Equilibrium
June 2006
pH 2.4-2.6
a
Saturation Index
-4
-2
0
2
4
6
8
Gib
Alu
Jar-H3O
Goet
Jar-K
Schw
Redoxcline
Solubility Equilibrium
April 2011
pH 2.8-3.0
b

Figure 12

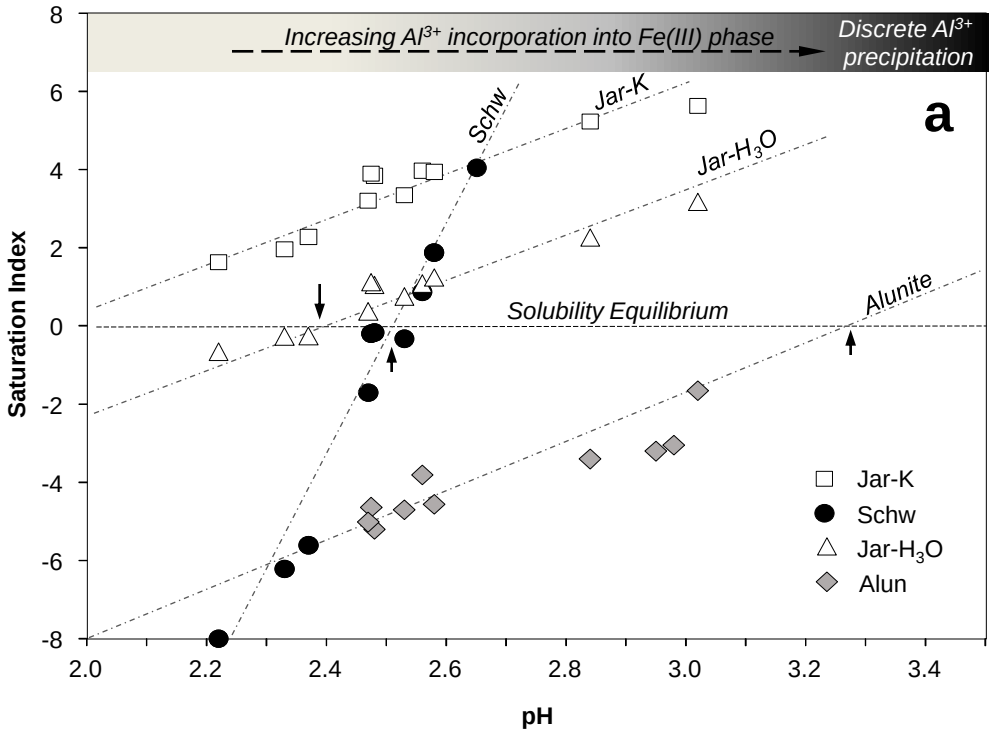
Increasing Al3+ incorporation into Fe(III) phase
Discrete Al3+ precipitation
a
Schw
Jar-K
Jar-H3O
Solubility Equilibrium
Alunite
Saturation Index
pH
Jar-K
Schw
Jar-H3O
Alun

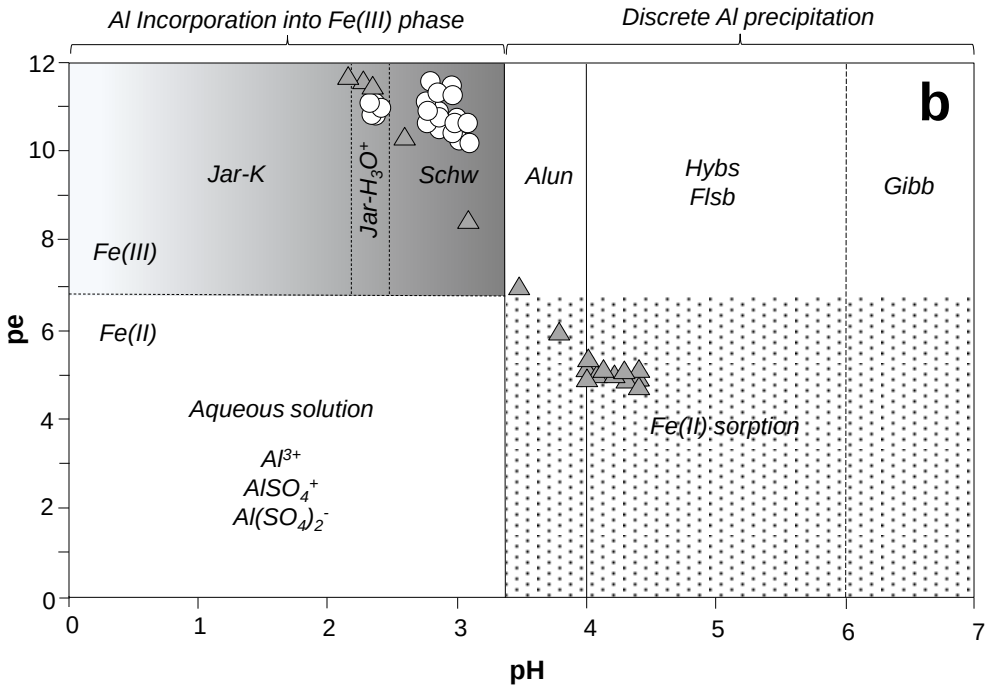
Al Incorporation into Fe(III) phase
Discrete Al precipitation
b
Jar-K
Jar-H3O+
Schw
Alun
Hybs
Flsb
Gibb
Fe(III)
Fe(II)
Aqueous solution
Al3+
AlSO4+
Al(SO4)2-
Fe(II) sorption
pe
pH

Figure 13